Multi-scale 3-dimensional characterisation of iron particles in dusty olivine: implications for paleomagnetism of chondritic meteorites

Multi-scale 3-dimensional characterisation of iron particles in dusty olivine: implications for paleomagnetism of chondritic meteorites

Joshua F. Einsle[1,2], Richard J. Harrison[1], Takeshi Kasama[3], Pádraig Ó Conbhuí [4], Karl Fabian[5], Wyn Williams[4] Leonie Woodland[7], Roger R. Fu[8], Benjamin P. Weiss[9], Paul A. Midgley[2]

AFFILIATIONS

1. Department of Earth Sciences, University of Cambridge, Downing Street, Cambridge CB2 3EQ, U.K.
2. Department of Materials Science & Metallurgy , University of Cambridge , 27 Charles Babbage Road, Cambridge CB3 0FS, UK.
3. Center for Electron Nanoscopy, Technical University of Denmark, Kongens Lyngby, Denmark
4. Grant Institute of Earth Science, University of Edinburgh, Kings Buildings, West Mains Road, Edinburgh, EH93JW, United Kingdom
5. Geological Survey of Norway, Leiv Eirikssons vei 39, 7491 Trondheim, Norway
6. CAGE - Centre for Arctic Gas Hydrate, Environment and Climate; Department of Geology, University of Tromsø, NO-9037 Tromsø, Norway
7. The Stephen Perse Foundation, Union Road, Cambridge, CB2 1HF, UK
8. Lamont-Doherty Earth Observatory, Columbia University, Palisades, NY, USA.

9. Department of Earth, Atmospheric and Planetary Sciences, Massachusetts Institute of Technology, Cambridge, MA, USA.

Abstract

Dusty olivine (olivine containing multiple sub-micrometer inclusions of metallic iron) in chondritic meteorites is considered an ideal carrier of paleomagnetic remanence, capable of maintaining a faithful record of pre-accretionary magnetization acquired during chondrule formation. Here we show how the magnetic architecture of a single dusty olivine grain from the Semarkona LL3.0 ordinary chondrite meteorite can be fully characterised in three dimensions, using a combination of Focussed-Ion-Beam nanotomography (FIB-nT), electron tomography and finite-element micromagnetic modelling. We present a three-dimensional (3D) volume reconstruction of a dusty olivine grain, obtained by selective milling through a region of interest in a series of sequential 20 nm slices, which are then imaged using scanning electron microscopy. The data provide a quantitative description of the iron particle ensemble, including the distribution of particle sizes, shapes, interparticle spacings and orientations. Iron particles are predominantly oblate ellipsoids with average radii 242 ± 94 nm by 199 ± 80 nm by 123 ± 58 nm. Using analytical TEM we observe that the particles nucleate on sub-grain boundaries and are loosely arranged in a series of sheets parallel to (001) of the olivine host. This is in agreement with the orientation data collected using the FIB-nT, and highlights how the underlying texture of the dusty olivine is crystallographically constrained by the olivine host. The shortest dimension of the particles is oriented normal to the sheets and their longest dimension is preferentially aligned within the sheets.

Individual particle geometries are converted to a finite-element mesh and used to perform micromagnetic simulations. The majority of particles adopt a single vortex state, with 'bulk' spins that rotate around a central vortex core. We observed no particles, which are in a true single domain state. The results of the micromagnetic simulations challenge some pre-conceived ideas about the remanence carrying properties of vortex states. There is often not a simple predictive relationship between the major, intermediate and minor axes of the particles and the remanence vector imparted in different fields. Although the orientation of the vortex core is determined largely by the ellipsoidal geometry (i.e., parallel to the major axis for prolate ellipsoids and parallel to the minor axis for oblate ellipsoids), the core and remanence vectors can sometimes lie at very large (tens of degree) angles to the principal axes. The subtle details of the morphology can control the overall remanence state, leading in some cases to a dominant contribution from the bulk spins to the net remanence, with profound implications for predicting the anisotropy of the sample. The particles have very high switching fields (several hundred mT), demonstrating their high stability and suitability for paleointensity studies.

1. Introduction

Chondritic meteorites have a long and complex formation history, involving condensation of primary minerals from the solar nebula, high-temperature processing during chondrule-forming events within the protoplanetary disk, accretion followed by thermal and/or aqueous metamorphism on the parent body, exposure to impact-related shocks, heating during passage through the Earth's atmosphere, weathering at the Earth's surface and hand magnet remagnetization during collection and curation (Weiss et al.

67 2010). This complexity makes chondritic meteorites particularly challenging from a
68 paleomagnetic perspective. Chondrites are magnetically heterogeneous on multiple
69 length scales ranging from metres to nanometres. Spatial variations in remanent
70 magnetization result from the presence or absence of magnetic fields at different stages of
71 their formation history. The challenge for paleomagnetists is to deconvolve the various
72 components of remanent magnetization, and determine the intensity and origin of the
73 magnetising fields.

74 Recent progress in this area has been driven by the development of scanning
75 SQUID microscopy (Weiss et al. 2007), which enables the remanent magnetic field of a
76 polished thin section to be measured with spatial resolution ~100 μm. Using a SQUID
77 microscope, combined with a non-magnetic microdrill, remanence measurements can be
78 made on mutually oriented sub-samples that are just a few tens of micrometres in size. By
79 focussing on these microscale regions of interest (MROI), the spatial heterogeneity of
80 magnetic remanence can be directly addressed and regions containing the most reliable
81 magnetic remanence carriers can be targeted for study. Although this approach offers the
82 only practical route to obtaining reliable paleomagnetic information from chondrites, it
83 comes at a high price: the smaller the volume of sample studied, the more its
84 paleomagnetic signal becomes dominated by the specific characteristics of remanence
85 carriers contained within it. For example, measurements made on a single silicate grain
86 are sensitive to the local anisotropic arrangement of remanence carriers, whereas such
87 local effects are averaged out in a bulk measurement. Interpreting paleomagnetic results
88 with confidence, therefore, requires a full three-dimensional characterisation of the
89 internal magnetic architecture of the MROI.

Here we describe how this goal can be achieved by using a Dual Beam Focused Ion Beam – Scanning Electron Microscope (FIB-SEM) to perform FIB-nanotomography (FIB-nT). The tomographic technique involves sequentially cross-sectioning through a selected MROI using the FIB and then imaging each cross-sectional face with the SEM (Holzer et al. 2004; De Winter et al. 2009; Schiffbauer and Xiao 2009; Bera et al. 2011; Keller et al. 2011a, 2011b; Holzer and Cantoni 2012; Landrot et al. 2012; Kruhl et al. 2013). The stack of high-resolution SEM images are then reassembled into a three dimensional (3D) volume, which is analysed quantitatively to extract the physical properties of the ensemble of particles. The 3D information is then used as the input to micromagnetic simulations that enable the magnetic properties of both individual particles and (in principle) the ensemble as a whole to be calculated.

We apply this method to a sample of 'dusty olivine' extracted from chondrules in the Semarkona LL3.0 ordinary chondrite, which recently formed part of a study to measure the strength of the magnetic field present during chondrule formation (Fu et al. 2014). The term 'dusty olivine' refers to grains of olivine containing numerous sub-micron inclusions of metallic Fe. Dusty olivines are thought to be relic grains of olivine that were caught up in a chondrule-forming event, heated (without melting) under reducing conditions to temperatures above the Curie temperature of the Fe inclusions, and then cooled in the presence of the nebular magnetic field (Connolly et al. 1998; Leroux et al. 2003; Hewins et al. 2005; Uehara and Nakamura 2006). Recent studies of synthetic analogues of dusty olivine, created by laboratory reduction of terrestrial olivine precursors, suggest that this material has the potential to maintain a faithful record of pre-accretionary remanence (Uehara and Nakamura 2006; Lappe et al. 2011, 2013).

However, these conclusions were primarily based on transmission electron microscopy (TEM) measurements of individual Fe particles in laboratory analogues (Lappe et al. 2011). TEM analysis requires thinning a sample to a foil less than 200 nm thick, thereby obscuring the original size, shape and spatial distribution of the magnetic remanence carriers. The approach put forward here, in contrast, preserves precisely the 3D information needed to reconstruct the magnetic architecture of the MROI. Furthermore, we apply this technique directly to natural dusty olivine samples.

2. Experimental Methods

2.1 Sample

The sample is a grain of dusty olivine extracted from a chondrule of the Semarkona LL3.0 chondrite (sample DOC5 from Fu et al. 2014). A full description of all sample preparation steps performed prior to our study is given by Fu et al. (2014). The sample was mounted on a quartz disk stub with epoxy, and the magnetic reference axes of the grain were marked. This enables the extraction of nanoscale information to be correlated back to the macroscopic magnetic measurements made by Fu et al. (2014). After optical investigation, the quartz disc was mounted onto a 38 mm SEM stub and carbon coated. Much of the sample surface was initially obscured by epoxy (Fig. 1a). Small bright specks visible in the exposed region of the grain correspond to the metallic Fe particles that define dusty olivine. FIB-nT was performed on the region highlighted in Fig 1a. The chosen region was adjacent to the region where a TEM lamella had previously been extracted from the olivine grain (Fu et al. 2014). The same TEM lamella was used to perform the additional TEM measurements reported here. The imaging

surfaces for both FIB-nT and TEM studies were acquired parallel to each other, allowing us to make direct comparisons across the length scales captured.

2.2 FIB-nT

FIB-nT was performed using a FEI Helios Nanolab Dual Beam microscope at the University of Cambridge. The sequential slicing and imaging sequence was controlled by the Auto Slice and View G3 (ASVG3) application. All FIB milling was performed using an accelerating voltage of 30 kV. The MROI was prepared by depositing a protective 10 μm by 15 μm by 1 μm tungsten pad using ion beam induced deposition with an ion beam current of 3 nA. The MROI was isolated from the bulk sample by selectively milling 20 μm deep trenches on three sides of the region defined by the W pad (Figs. 1b – d) using a 7 nA ion beam current. The front trench allows full viewing access to the cross sectional surface and the side trenches minimize re-deposition effects associated with the sequential sectioning process. Figure 1b shows the tomographic region of interest immediately after clearing away excess material. Finally, a pair of fiducial marks was created before starting the automated sequence, using the 3 nA ion aperture for W deposition and 300 pA aperture for feature milling. Figure 1c is a FIB micrograph used for slice placement, showing the actual field of view used, taken at an arbitrary point in the automated slice-and-view routine. The fiducial mark seen in Figs. 1b and 1c controls the placement of each slice of the tomographic sequence, whereas the fiducial mark seen in Fig. 1d minimizes the amount of image drift in the SEM image stack. Each 20 nm thick tomographic slice was milled away using a 920 pA ion beam current. All milling was performed at 52° stage tilt, which is normal to the FIB.

158 Each image of the tomographic sequence was recorded using a dwell time of 20
159 μs with an 8 bit grey scale and a scan area of 1024 by 884 pixels. The horizontal field
160 width of the final image was set to 10 μm. This gave a final pixel size of 9.766 nm.
161 Imaging of the cross-sectional cut face was achieved using back-scattered electron (BSE)
162 imaging with the SEM operating in immersion mode at a low accelerating voltage of 2
163 kV with a beam current of 86 pA. We used the through the lens detector in back-scattered
164 electron mode for the strong material contrast mechanism between the olivine host matrix
165 (dark grey) and the Fe nanoparticles (bright greys) (Fig 2a). This combination of through
166 lens detection and backscatter mode also eliminates contrast artefacts like shadowing and
167 allows for higher spatial resolution over Everhart-Thornley detector geometries. SEM
168 imaging conditions were further optimized to reduce noise in the BSE image as well as to
169 ensure that only the cross-sectioned surface was imaged. Reduction of the electron
170 interaction volume was achieved by using the low accelerating voltage of 2 kV. Detector
171 noise in the image was minimised by reducing the working distance from 4 mm to 3.3
172 mm. Additionally, to protect the pole piece at the shorter working distance the sample
173 was tilted to 47.8°. Movement between the SEM imaging position and the FIB patterning
174 position was controlled automatically through ASVG3. Using this automation routine,
175 262 slices were recorded over 15.3 hours, with a specified slice thickness of 20 nm
176 resulting in a total milled thickness of 5.2 μm.
177

178 **2.3 Image Post-Processing**

179 Data post-processing and analysis were performed using a combination of the
180 commercial package ORS Visual SI and the open-source platform FIJI, based on the

ImageJ image analysis distribution (Schindelin et al. 2012). The 262 images were loaded as a single three-dimensional image stack into ORS Visual SI. The pixel aspect ratio was adjusted to correct for the sample tilt and the slice thickness of 20 nm was applied to the image stack. This resulted in voxel dimensions of 9.8 nm by 13.2 nm by 20 nm. Although the fiducial mark seen in Fig. 1b helps to minimize image stack drift, erosion of this feature during the sequential milling of the MROI resulted in a progressive drift in the final image position on the cut face. Applying the Normalized Mutual Information alignment algorithm within ORS Visual SI the image stack alignment tool allowed for precise and jitter-free alignment of the reconstructed volume.

The image stack was segmented to define the Fe particles and olivine matrix (Fig. 2a). Several approaches for this have been documented in the literature (Holzer et al. 2004; Bushby et al. 2011; Keller et al. 2011a). We found that the best results were obtained using simple greyscale thresholding followed by noise reduction and manual artefact removal. Middle grey levels (114 – 212) associated with Fe particles were assigned a saturating value of 255. All other pixels were set to 0. After applying this binary segmentation, residual detector noise was eliminated by one pass of the FIJI/ImageJ despeckle filter. Next, residual W deposition, milling curtain artefacts and particles partially lying on the edges of the reconstructed volume were manually removed from the image stack. Close inspection of the original images revealed saturated black and saturated white pixels around some Fe particles. It is thought that these are pockets of silica glass formed as a by-product of the solid-state reduction reaction that created the Fe particles (Leroux et al. 2003). As these regions are non-conductive, they tend to induce charging effects in the images registering as saturated white. Related to these are

saturated black voxels that upon inspection of the original image stack can be seen to be either non-charging glass (which charge up in subsequent images) or holes in the olivine crystal. The holes and charging artefacts can be seen in Fig. 2a. Grey scale binary segmentation does not fully isolate the Fe particles from these parasitic features and so these regions were manually removed from the segmented images. Fig. 2b shows the same image after binary segmentation and manual artefact removal.

Quantitative three-dimensional analysis of the resulting scaled aligned and segmented image stack was performed using the ImageJ/FIJI plug-in BoneJ version 1.3.15 (Doube et al. 2010; Carriero et al. 2014). The BoneJ Particle Analyser generates a surface mesh for each particle and determines a best-fitting ellipsoid to that surface. Errors in the ellipsoid fitting are of the order of the voxel size and therefore can become significant for particles that are defined by a small number of voxels. Additionally non-physical results were obtained for groups of voxels that appeared only on one image of the stack. These voxel groups consisted of either segmentation noise that was not fully removed, or very small particles with radii less than 20 nm in one dimension (i.e., these are particles that are less than the thickness of a tomography slice). This establishes our 3D resolution limits and means we do not observe any particles with a diameter of less than 40 nm. However, TEM studies did not reveal any particles smaller than this. After artefact removal we were left with 246 particles in the 710 μm3 volume analysed by FIB-nT.

2.4 TEM

To complement the mesoscale tomographic information provided by FIB-nT, we also performed high-resolution TEM studies of individual particles using scanning

227 transmission electron microscopy (STEM). The TEM lamella was fabricated using FIB
228 milling (Fu et al. 2014). All studies were performed at the Technical University of
229 Denmark (DTU) on an FEI Titan 80-300 TEM equipped with a field-emission electron
230 source, monochromator, spherical aberration probe corrector, Lorentz lens and
231 electrostatic biprism. All measurements were made using 300 kV accelerating voltage.
232 Preliminary Lorentz microscopy and electron holography observations were reported by
233 Fu et al. (2014).

234 Here we present bright-field TEM and STEM imaging, electron diffraction data as
235 well as dark-field STEM tomography results. Both TEM and bright-field STEM modes
236 allow us to image crystallographic features such as dislocations and sub-grain boundaries
237 (Williams and Carter 2002; Crewe and Nellist 2009). Dark-field STEM tomography of a
238 single particle was performed using a camera length of 130 mm to produce a strong
239 material contrast between the Fe particles and the olivine crystal. The tomographic series
240 was collected at a magnification of 28500X (giving a pixel size of 3.26 nm) using the
241 high angle annular dark field (HAADF) detector. The tilt series consisted of an image
242 taken every 2° for tilts from -76° to +76°. Alignment and reconstruction of the tilt series
243 was achieved using Inspect 3D with the SIRT algorithm (Gilbert 1972). Visualisation
244 was performed using Avizo Fire.

245

246 **2.5 Micromagnetic Modelling**

247 A selection of Fe metal particles, representing the range of sizes and shapes
248 within the ensemble, were chosen to perform detailed micromagnetic simulations. Each
249 particle was cropped from the segmented FIB-nT stack and converted to a tetrahedral

250 finite-element mesh in a multi-step process. An example of the initial geometry of a
251 particle defined by the FIB-nT is shown in Fig. 3a. Each rectangular block represents a
252 single 9.8 x13.2 x 20 nm voxel. This representation of the particle was used to generate a
253 bounding polyhedron that best approximates the actual particle surface, where each point
254 of the resulting mesh must solve a Poisson boundary condition (Fig 3b). We further
255 refine the surface mesh by passing it through a surface smoothing routine (Fig. 3c). We
256 coarsen the smoothed surface using a Delaunay triangulation routine to produce a surface
257 mesh at the desired resolution of 5 nm (Fig. 3d). The final triangular surface mesh was
258 imported into the software package CuBit (KitWare), where it was turned into a
259 tetrahedral volume mesh. We used an initial surface mesh with average node spacing 5
260 nm, which was then used to generate tetrahedral nodes on average every 5 nm throughout
261 the volume. Although this resulted in a mesh size slightly bigger than the 3.4 nm
262 exchange length for iron, it enabled the number of elements in the model to be kept
263 below approximately 300,000 and provides acceptable resolution for modelling simple
264 vortex micromagnetic structures.
265 Micromagnetic modeling was performed using MERRILL (Micromagnetic Earth
266 Related Rapid Interpreted Language Laboratory), a micromagnetics package optimized
267 for the rock magnetic community developed by K. Fabian and W. Williams (Williams
268 and Fabian 2016). MERRILL uses a Finite Element Method/Boundary Element Method
269 (FEM-BEM) to solve for the magnetic scalar potential inside the particle and thereby
270 calculate the demagnetizing energy of the system. The use of FEM-BEM avoids the need
271 to discretize the non-magnetic volume outside the particle. Simulations were performed
272 by minimizing the total micromagnetic energy. This consists of summing the exchange,

273 cubic anisotropy, magnetostatic and demagnetizing energies. Energy minimization was
274 performed using a conjugate gradient method, specially adapted to micromagnetic
275 problems. MERRILL has been successfully tested against μMAG Standard Problem #3
276 (http://www.ctcms.nist.gov/~rdm/mumag.org.html).

277 Material parameters used were appropriate for pure iron at room temperature:
278 saturation magnetization M_s = 1715 kA/m, exchange constant A = 2 x 10^{-11} J/m, and
279 cubic anisotropy with K_1 = 48 kJ/m^3 (Muxworthy and Williams 2015). We arbitrarily set
280 the cubic <100> axes parallel to the X, Y and Z axes of the volume reconstruction. We
281 will show in Section 3.3 that this does not greatly influence our analysis, as the magnetic
282 behavior of the particles studied is dominated by shape rather than magnetocrystalline
283 anisotropy.

284 Using the method of Hubert (1967), it can be estimated that magnetostrictive
285 effects become important for iron only when the magnetostrictive energy density 9/2 (c_{11}-
286 c_{12}) λ_{100}^2 is of similar size as the energy density ~2(A K_1)$^{1/2}$ /d generated by a 180º-domain
287 wall, where d is the dimension of the particle (Hubert 1967; Fabian et al. 1996; Hubert
288 and Schäfer 1998). For iron with elastic constants c_{11}=241 GPa, c_{12}=146 GPa (Lee 1955),
289 and λ_{100}=22 x10^{-6} (Radeloff 1964), this occurs only for d >9 μm such that
290 magnetostriction can safely be neglected for all modeled particles. Also magnetoelastic
291 interaction is neglected because it is assumed that any strain involved in the formation of
292 the particles has been relaxed by plastic deformation such that no noticeable internal
293 stress field is present.

294 Simulations were performed using an Apple iMac with a 3.4 GHz Intel i7
295 processor and 24 GB of RAM. Each particle was initialised with uniform magnetization

along either the X, Y and Z axes of the reconstructed volume. Fields varying from 1000 mT to -1000 mT in steps of 10 mT were applied along X, Y and Z. The converged set of magnetic moments obtained after each field step was subjected to small random rotations (maximum angle 20°) and then used as the basis for the starting condition for the next field step. This step is to insure that the energy minimisation is not trapped in a local energy minima. The average magnetization projected on each of the X, Y, and Z axes were calculated at each step in order to generate the upper branch of the hysteresis loop. Lower branches were not calculated directly using micromagnetics, but are presented for visualisation purposes under the assumption that these are symmetrically equivalent to the upper branch.

3. Results

3.1 FIB-nT

The reconstructed dusty olivine volume is shown in Fig 4a-c. A qualitative analysis (see movie in supplemental information) reveals that i) the particles are loosely arranged in planar sheets, ii) the particles tend to be flattened in the direction perpendicular to the sheets, and iii) there is a preferred orientation of particle elongation along a direction within the sheets. We will present the crystallographic analysis in section 3.2 when we present the TEM and STEM results. Particles are widely distributed in terms of their size and aspect ratio. Figure 5 summarises this distribution by plotting a histogram of the best-fit ellipsoid diameters for the major (Fig. 5a), intermediate (Fig. 5b) and minor (Fig. 5c) axes. The average particle radii are 242 ± 94 nm by 199 ± 80 nm by 123 ± 58 nm. In order to classify the particles in terms of their tendency towards either

318 uniaxial prolate or uniaxial oblate symmetry, we plot the aspect ratio of the major to
319 intermediate radii against the aspect ratio of the intermediate to minor radii in Fig. 6a
320 (Flinn 1962). This 'Flinn' plot also scales the size of each data point to the size of the
321 major radius. The line $y = x$ separates prolate particles (above the line) from oblate
322 particles (below the line). There are significant populations of small, flattened particles
323 that plot close to the horizontal (uniaxial oblate) and elongated particles that plot close to
324 the vertical (uniaxial prolate) axes. As seen qualitatively in the Flinn plot and
325 quantitatively in the histogram in Fig. 6b, 95% of the particles are classified as oblate in
326 aspect ratio with a mean Flinn ratio of 0.76. This gives the majority of particles a tri-axial
327 symmetry. This non-spherical and non-uniaxial aspect ratio has profound implications for
328 the magnetic anisotropy of each particle, which we will explore in more detail using FEM
329 models (Section 4.3). Of the reconstructed particles, only 11 possess a prolate aspect
330 ratio. The three smallest of these are close to the limitations of our reconstruction
331 resolution. For these particles, the radii are between 2 to 6 voxels long in any one
332 direction, which means that the uncertainty in the ellipsoid-fitting algorithm can be on the
333 order of the size of the particle. We found that extracting these individual particles from
334 the larger tomographic volume and rerunning the BoneJ analysis lead to small changes in
335 the fitted ellipsoid parameters, causing them to be reclassified as oblate. Reported
336 population statistics refer to the results of the whole ensemble fitting, which are accurate
337 for all but these very small particles.
338 The orientations of major, intermediate and minor ellipsoid axes are shown in Fig.
339 7. All three axes show pronounced clustering of their principal axes, confirming the
340 qualitative assessment above (note that the ellipsoid fitting does not distinguish between

positive and negative vectors). The minor ellipsoid axes (blue circles) are tightly clustered in the direction normal to the sheets, whereas there is a much broader spread of major and intermediate axes within the sheets (red and green circles, respectively). Solid triangles in Fig. 7 show the principal axes of the anisotropy of susceptibility of anhysteretic remanent magnetization (ARM) for the whole dusty olivine chondrule, as determined by scanning SQUID microscopy (Fu et al. 2014). The coordinate system used for reporting results is based around the orientations of the FIB-SEM microscope. We have transformed the coordinates Fu et. al. (2014) to agree with the microscope system. The average orientation of the major ellipsoid axes coincides with the direction of highest ARM susceptibility, whereas the intermediate and minor susceptibilities lie at angles of ~40° from the average orientations of the intermediate and minor ellipsoid axes, respectively.

3.2 TEM and STEM analysis

Fig. 8a shows a bright-field STEM mosaic of the entire lamella. The prominent dark feature running horizontally along the top of the image is the remains of the Pt capping layer that was deposited on the surface of the sample to protect it during FIB milling. The Pt layer became partially detached from the surface after the lamella was plasma cleaned prior to insertion in the TEM. The Fe particles appear dark against the mid grey olivine background. Silica glass regions appear as light grey blebs parasitic to the Fe particles. Electron diffraction patterns were obtained for the olivine and Fe particles inside the red-boxed region shown in Fig. 8a. Figure 8b has been oriented with respect to the region highlighted in larger montage image. The upper right hand

364 diffraction pattern in Fig 8b was collected from olivine in this region with an α-tilt of -
365 3.5° and a β-tilt of -1.1°, and corresponds to a [130] zone axis (~9° from [010]). The
366 diffraction pattern in the lower left corner of Fig 8b was obtained from the smaller of the
367 two Fe particles with an α-tilt of 8.8° and a β-tilt of -6.8°, and corresponds to a [001]
368 zone axis. The short axis of the particle corresponds to the [100] direction of Fe and lies
369 normal to the (001) plane of olivine. This is in agreement with the orientation data
370 collected using the FIB-nT (inset upper left), and highlights how the underlying texture of
371 the dusty olivine is crystallographically constrained by the olivine host.
372 The lower right hand image in Fig. 8b is a 3D visualisation of the small Fe
373 particle obtained using STEM tomography (Movie of particle in Supplemental
374 Materials). The voxel size is 3.3 nm, at least a factor of 3 smaller than the voxel size
375 obtained via FIB-nT. The particle dimensions are 232 nm by 205 nm by 232 nm (X, Y, Z
376 with respect to the image plane), giving it a slightly oblate profile. These dimensions
377 mean that the particle is one of the smaller ones in the population. It is representative of
378 the largest complete particle that could be imaged using STEM tomography (larger
379 particles were truncated by the surfaces of the TEM foil). Particles of this size (and
380 smaller) are observable using the FIB-nT approach (albeit at considerably lower spatial
381 resolution), so there is some overlap between the size ranges accessible by the two
382 techniques. 2D particle analysis of this lamella does not reveal any particles smaller than
383 those observed in the FIB-nT volume.
384 Figure 8a shows sub-grain boundaries in the olivine running parallel and
385 perpendicular to [001]. As the diffraction pattern for the olivine in Fig 8b is oriented with
386 respect to Fig 8a, we see that the olivine's [001] is perpendicular to the sharp sub-grain

boundaries. In contrast, the sub-grain boundaries running parallel to the [001] are slightly blurred. This broadening we interpret to be the result of the trace of the (010) intersecting the 100 nm thick lamellae surface with an angle of around 9° as noted above. These observations about the arrangement of the sub-grain boundaries are in line with the previous study by Kirby and Wegner (1978), which demonstrated that the dislocation arrays in olivine concentrate along the {100} lattice planes. The dislocations defining the sub-grain boundaries are more clearly visible in the bright-field TEM image (Fig. 8c), which was taken from the region outlined in blue. The sub-grain boundary seen on the right of this image is parallel to (001) of the olivine and lies parallel to a prominent (100) facet of the Fe crystal. This sub-grain boundary is also parallel to the plane containing the major and intermediate axes of the ensemble (inset upper left). Previous studies of natural and synthetic dusty olivines (Leroux et al. 2003; Lappe et al. 2013) have suggested that the Fe nanoparticles arrange along dislocation arrays associated with the sub-grain boundaries. By measuring the crystallographic information of the lamella from the same region, we are able to demonstrate that the particle ensemble does indeed arrange in sheets related to crystallographic planes of the olivine host crystal.

3.3 Micromagnetic Simulations

3.3.1 Remanence states and magnetic moments. The results of micromagnetic simulations for 9 selected particles (8 particles extracted from the FIB-nT stack plus the STEM tomography particle shown in the red inset of Fig. 8) are summarized in Table 1. A range of oblate (Flinn ratio less than 1) and prolate (Flinn ratio greater than 1)

410 ellipsoids are represented, with volumes ranging from the smallest in the ensemble
411 (Particle 48) to those closer to the average (Particle 165). Remanence states were
412 obtained after applying a saturating field of 1 T along the X, Y and Z directions of the
413 reconstructed volume, and then stepping the field down to zero in steps of 10 mT. The
414 squareness M_{rs}/M_s is the magnitude of the total remanence vector normalized to the
415 saturation moment of the particle. To aid comparison and to give a better sense of the
416 magnitude of the magnetic moment of each particle, we define 'relative M_r' as the total
417 remanent moment of the particle divided by the total remanent moment of a uniformly
418 magnetized 25 nm diameter sphere. This size corresponds to the upper threshold for
419 single-domain (SD) Fe (Muxworthy and Williams 2015).

420 No particles were small enough to adopt an SD state. Instead all particles adopt
421 either pseudo-single domain (PSD) or emerging multi-domain (MD) states, consisting of
422 either a single vortex or multiple vortex/wall-like structures (Fig. 9). To highlight the
423 orientation and nature of vortex cores, the magnitude of the vorticity of the moment
424 vector field ($|\nabla \times \boldsymbol{M}|$) is plotted as an isosurface (green in Fig. 9). The choice of isosurface
425 magnitude is somewhat arbitrary (too large and only the ends of the core are highlighted;
426 too small and the surface extends too far from the core region). We chose the largest
427 value that would produce a continuous trace of the core from one surface termination to
428 another. The remanent states of the particles studied can be divided into four general
429 categories: I) single vortex with core oriented close to the minor axis of the best-fitting
430 ellipsoid (Fig. 9a); II) single vortex with core oriented within the plane defined by the
431 minor and major axes of the best-fitting ellipsoid (Fig. 9b); III) single vortex with core

oriented parallel to the major axis of the best-fitting ellipsoid (Fig. 9c); IV) multiple vortex/wall-like structures containing two or more cores (Fig. 9d).

Type I behavior was typically observed in oblate particles with lower Flinn ratios (flattened ellipsoids). Type I particles display straight cores located at the center of the largest face. The relatively strong demagnetizing field of the vortex core in this case can be shielded by antiparallel spin tilting at the outer rim of the oblate particle. Type II behavior was typically observed in oblate particles with higher Flinn ratios (triaxial ellipsoids). Type II particles display curved cores that adopt a sigmoidal trajectory through the center of the particle. The ends of the core lie normal to their surface terminations, as requested by the micromagnetic boundary conditions (e.g., Hubert and Schäfer 1998). Type III behavior was observed in the three prolate particles. Type III particles display cores that track the major ellipsoid axis in the central section of the particle. The ends of cores again lie normal to their surface terminations, causing deviations and distortions of their trajectory. Type IV behavior was observed in the two large prolate particles and already represents a diamond-shape domain pattern with preference for 90° walls, as previously observed for iron thin films and whiskers (e.g., Fig. 5.94 in Hubert and Schäfer, 1998). The remanent state of these particles was more sensitive to the direction of the saturating field than oblate particles with similar volume. In the case of Particle 233 (the largest and most elongated prolate particle), states III, IVa and IVb were adopted for saturating fields applied along X, Y and Z, respectively (Table 1). IVa contains two curved cores corresponding to Bloch walls that split the particle into magnetic domains; IVb is an efficient flux closure structure containing ten magnetic domains (Fig. 9d).

455 The morphology of the vortex core evolves with increasing volume of particle
456 (Fig. 10). Small particles contain well-defined cylindrical cores (Fig. 10a). Larger
457 particles develop cores with a 'winged' structure, with wings protruding along the
458 directions of emerging domain walls (Fig. 10b). In larger prolate particles, the core is
459 poorly defined, becoming flattened and developing off-shoots (Fig. 10c) and loops (Fig.
460 10d), suggestive of emerging MD behavior.
461 The emerging walls can be better defined and visualized as isosurfaces of the
462 magnetocrystalline anisotropy energy, which highlights those regions where the
463 magnetization points away from the <100> magnetocrystalline easy axes (Fig. 11). As
464 before, the choice of isosurface magnitude is somewhat arbitrary (too large and the
465 domain walls develop holes; too small and the walls become unreasonably wide). We
466 chose a value that generated the thinnest continuous wall structures. Examining the
467 remanent state for each of the orthogonal magnetization directions, a variety of domain
468 wall-like behaviors can be identified. Fig. 11a depicts the Type III remanent state
469 observed after applying saturating fields along X. A cross section through the anisotropy
470 surface of this state is shown in Fig. 11c. The cross section reveals the presence of 4 wall-
471 like structures associated with the rotation of spins around a central vortex core. Due to
472 its alignment with a perpendicular easy axis, the vortex core appears as the cylindrical
473 hole in the center of the anisotropy surface in Fig. 11c. Near the particle center, the
474 domain walls tend to be thinner and better defined. Walls broaden towards the particle
475 surface, as the magnetization adapts to the surface morphology, driven by the need to
476 avoid high magnetostatic energy. Figs. 11b and d show Type IVa and IVb behavior,
477 revealing the presence of well-defined 90° domain walls. Again, there is a tendency for

478 domain walls to be thinner in the grain interior, broadening and adopting a more Néel-
479 like character as the spins adapt to the surface morphology (Hubert and Rave 1999).
480
481 **3.3.2 Remanence vectors with respect to particle shape.** Stereograms showing the
482 predicted remanence vectors obtained after applying fields along X (black circle), Y
483 (black square) and Z (black triangle) are shown in Fig. 12 for selected particles. Also
484 shown are the orientations of the minor, intermediate and major axes of the best fitting
485 ellipsoids (blue, green and red diamonds, respectively), and the corresponding traces of
486 the planes normal to these directions. For single vortex states, the remanence vector is
487 dictated primarily by the magnetization of the vortex core, but the precise remanence
488 direction is modified significantly by switching the sense of rotation of the bulk spins.
489 Denoting the core direction as either up or down and the sense of bulk spin rotation as
490 being either left or right, this results in two pairs of distinct remanence directions for each
491 particle: (up left and down right) and (up right and down left) (Fig. 12a). The remanence
492 states in each pair are antiparallel to each other, but lie at some angle to the other pair.
493 Remanence directions for two Type I particles are shown in Figs. 12b and 12c. The angle
494 between remanence pairs is 32° for Particle 364 (Fig. 12b) and is 80° for Particle 155
495 (Fig. 12c). In Particle 364 (a small oblate particle), the remanence lies close to the core
496 direction, i.e. close to the minor axis of the best-fitting ellipsoid (Fig. 12b). Note also that
497 the remanence states obtained for this particle after applying a saturating fields along X
498 and Z are identical (only the X state is plotted in Fig. 12b). In Particle 155 (the most
499 extreme oblate particle), the remanence obtained after magnetizing along Y lies much
500 closer to the major axis of the best fitting ellipsoid than the minor axis (Fig. 12c). A Type

501 II particle is shown in Fig. 12d. The angle between remanence pairs is small (16°) and the
502 remanence lies at an intermediate angle between the minor and major axes of the best
503 fitting ellipsoid, parallel to the average core orientation. A Type III particle is shown in
504 Fig. 12e. The angle between remanence pairs is 56°, with the remanence lying close to
505 the minor axis for fields applied along X and close to the major axis for fields applied
506 along Z. In Type IV particles (not shown), the remanence generally lies closest to the
507 major axis of the best-fitting ellipsoid. Those particles that show a change of domain type
508 with field direction (Table 1) display a correspondingly wider range of possible
509 remanence directions.

510 It is possible to access each of the four states by applying a suitably oriented
511 saturating field. For example, applying saturating fields to Particle 155 along X and Y
512 switches the sense of vortex rotation while retaining the direction of core magnetization
513 (Fig. 12c). In small fields, the four states are separated by energy barriers that could, in
514 principle, be overcome by thermal fluctuations. However, the energy barriers associated
515 with switching the sense of vortex rotation while retaining the core direction (or
516 switching the core direction while retaining the sense of vortex rotation) are likely to be
517 very high compared to the barriers associated with switching both together. This is
518 because the former process will require considerable internal disruption to the
519 micromagnetic state and a correspondingly high exchange energy penalty, while the latter
520 can be achieved simply by 180° rotation of the micromagnetic state against the shape
521 anisotropy of the particle. Calculating these energy barriers is the next computational
522 challenge, and will ultimately enable the acquisition of remanence during cooling of
523 these particles to be modelled.

524

525 **3.3.3 Hysteresis loops.** Hysteresis loops are shown in Fig. 13 for selected particles and
526 applied field directions. The magnetic response of all particles is dominated by reversible
527 magnetization processes (e.g., the rotations of bulk spins towards the field). The
528 reversible component of magnetic susceptibility is highest (lowest) for fields applied
529 parallel to the major (minor) axis of the best-fitting ellipsoid. Irreversible magnetization
530 processes (e.g., nucleation of vortices, irreversible switching of vortex core position, core
531 orientation or core magnetization, changing sense of bulk spin rotation, denucleation of
532 vortices) produce small steps in magnetization superimposed on the large reversible
533 component. This leads to loops characterized by very low values of coercivity (H_c) and
534 squareness (M_{rs}/M_s). Highest coercivities (30-40 mT; Table 1) are observed in the small
535 Type 1 particles when fields are applied along X (e.g., antiparallel to the core direction,
536 close to the minor axis of the best-fitting ellipsoid; Fig. 13a). Typical coercivities are of
537 the order of a few mT or less (Fig. 13d). Negative values of coercivity listed in Table 1
538 highlight an unusual behavior (e.g., Fig. 13c), whereby the upper branch of the hysteresis
539 curve reaches the M = 0 axis at a positive applied field. This behavior leads to a self-
540 reversal of saturation isothermal remanent magnetization (SR-SIRM), in which a
541 component of saturation remanent magnetization is antiparallel to the saturating field
542 direction.

543 Despite the low M_{rs}/M_s values, the large volume of the particles means that their
544 total moments are at least equivalent to that of a 25 nm diameter SD particle, and in many
545 cases significantly greater (relative M_r values vary from ~1 up to ~44; Table 1). Despite
546 the low H_c values, the remanence states are also highly stable with respect to applied

547 fields. We define the stability of a remanence sate in terms of the 'minimum irreversible
548 field' (Table 1). To calculate this field, the spin state obtained at each negative field of
549 the upper hysteresis branch (from -10 to -1000 mT) was chosen as an initial
550 configuration, and the micromagnetic energy was minimized under zero field. The
551 minimum irreversible field is the smallest negative field required to produce a change in
552 the remanent state of the particle. Minimum irreversible fields are typically several
553 hundred mT, with several showing remanence states stable to more than 400 mT and one
554 simulation showing no significant change even up to 1000 mT. Note that the coercivity of
555 remanence (H_{cr}) is greater than or equal to the minimum irreversible field. Based on the
556 values in Table 1, all particles would plot in the MD region of a Day-Dunlop plot
557 (Dunlop 2002). However, such a comparison grossly misrepresents the remanence
558 carrying potential of these particles. Although the ratio of H_{cr}/H_c is similar to MD
559 samples, which make notoriously poor paleomagnetic recorders, the absolute values of
560 H_{cr} are at least an order of magnitude larger. Furthermore, MD materials have vanishingly
561 small values of the minimum irreversible field, since irreversible changes to the remanent
562 state of an MD material can be achieved by movement of weakly pinned domain walls.
563 For the vortex states studied here, no changes whatsoever are observed in the remanence
564 state until fields of several hundred mT are applied. A better comparison of the
565 remanence carrying potential of vortex states is obtained by first-order reversal curve
566 (FORC) analysis, which is not adversely affected by the large component of reversible
567 magnetization associated with the rotation of bulk spins. The range of irreversible fields
568 calculated here corresponds very well to the distribution of irreversible magnetization
569 observed in synthetic dusty olivine samples using FORC diagrams (Lappe et al. 2011,

570 2013) and to the high stability of natural remanent magnetization with respect to
571 alternating-field demagnetization observed by Fu et al. (2014). In comparison, FORC
572 diagrams of MD materials typically show irreversible magnetization restricted to fields
573 less than a few mT (Church et al. 2011; Lindquist et al. 2015) Unsurprisingly, the lowest
574 irreversible fields observed here are for Type IV particles, which contain more MD-like
575 structures. Even here, though, irreversible fields of 40-100 mT are typical.
576

577 **4. Discussion**

578 **4.1. Rock magnetism of realistic ensembles**

579 Conventional characterisation of the remanence carriers in rocks typically relies
580 on either optical or SEM imaging of polished surfaces, or TEM imaging of thin foils.
581 Although such 2D methods are an essential part of the qualitative characterisation
582 process, our numerical simulations emphasise just how important 3D knowledge of
583 particle geometry is for quantitative modelling. Shape and crystallographic orientation of
584 an individual particle controls the orientation of its vortex core, or equivalently the
585 position and type of its domain walls. Near the surface the bulk spins adapt to the
586 faceting of the particle. In symmetric particles, we might expect that the bulk spins cancel
587 each other out and that the total remanence would be dominated by uncompensated spins
588 within the core. A striking example of where this assumption breaks down is shown in
589 Fig. 14 (Particle 155, a Type I particle with a pronounced oblate geometry). In this case,
590 the core is parallel to the minor axis of the best-fitting ellipsoid, but the net remanence
591 lies at a large angle to this, and rotates by 80° as the sense of bulk spin rotation changes

592 (Fig. 12c). The explanation for this behaviour is the combination of the short length of
593 the core, which reduces its contribution to the net moment, and the uneven length of
594 opposing surface facets, which creates a significant contribution from uncompensated
595 bulk spins. In Fig. 14, this unbalancing is highlighted by plotting the anisotropy energy of
596 the domain walls. The width of the walls and the sizes of the four resulting quadrants can
597 be seen to be of unequal sizes. In the configuration shown, there are more spins pointing
598 along +Z due to the larger facet on right than there are compensating spins along –Z due
599 to the small facet on the left. A similar situation is known for vortex states in sufficiently
600 large uniaxial particles, where several metastable magnetization states may exist that are
601 related to edge moments that can be aligned parallel or anti-parallel to the global
602 demagnetizing field (Fig. 7 in Rave et al. 1998). The importance of bulk spins in
603 controlling the remanence of vortex states in particles with realistic morphologies is not
604 generally appreciated.
605 The sheet-like arrangement of particles within the reconstructed volume (Fig. 4) is
606 expected to generate significant remanence anisotropy. Such anisotropy is well
607 documented in single-crystal paleomagnetism studies (Feinberg et al. 2004, 2005; Fu et
608 al. 2014) and must be corrected before the measured remanence directions can be
609 interpreted quantitatively. Fu et al. (2014) measured the anisotropy of ARM susceptibility
610 for the same grain studied here (Fig. 7), finding normalised values of 0.45, 0.56 and 1 for
611 the minimum, intermediate and maximum susceptibilities, respectively. The maximum
612 ARM susceptibility is observed for fields applied along Z, which corresponds to the
613 average orientation of major ellipsoid axes. This observation is most consistent with
614 remanence carried by prolate Type III and IV particles and oblate Type I particles such as

615 those shown in Fig. 14, and suggests that such particles are more prevalent in regions of
616 the grain outside the reconstructed volume. The fact that the minimum susceptibility axis
617 is not aligned with the average orientation of minor axes is explained by the presence of
618 Type I and II particles, which contribute to the remanence when fields are applied normal
619 to the sheets. A full model of the entire ensemble, taking into account the magnetostatic
620 interaction fields between particles and the distribution of shape anisotropy, would be
621 necessary to fully describe the anisotropic response of the system (Hargraves et al. 1991)
622 as well as accounting for the presence of much larger particles that may occur outside the
623 analysed volume. Such calculations could serve to improve dramatically the
624 interpretation of single-crystal paleomagnetic studies, and minimise the number of repeat
625 measurements needed to reach a statistical significance equivalent to bulk paleomagnetic
626 studies.
627

628 **4.2 Implications for chondrite paleomagnetism**

629 This study demonstrates that particles in the lower half of the size distribution
630 adopt a single vortex state (Type I and II), with the larger particles adopting Type III and
631 IV (i.e., emerging MD) behaviour. Lappe et al. (2011) similarly identified a dominance of
632 single vortex states, but noted also a significant number of SD particles. It appears that
633 the size distribution of particles in synthetic dusty olivine is shifted to smaller values than
634 the natural sample studied here. Nevertheless, given the abundance of single vortex states
635 in both cases, calibrations of non-heating paleointensity methods using synthetic dusty
636 olivine (Lappe et al. 2013) remain largely valid. Similarly, given the high field stabilities
637 observed here for single vortex states (Table 1), the conclusion that dusty olivine is

638 capable of recording and maintaining a faithful record of pre-accretionary remanence
639 (Lappe et al. 2011) also remains valid. Indeed, the combination of high switching fields
640 and large volumes of single vortex states should translate to carriers with very high
641 thermal stability (i.e. high blocking temperatures). High thermal stability of vortex states
642 at temperatures up to the Curie temperature has recently been demonstrated in magnetite
643 using electron holography(Almeida et al. 2014, 2016). In principle, micromagnetic
644 simulations can be used to calculate energy barriers between alternate remanence states,
645 and thereby model the acquisition of thermoremanent magnetization. Such calculations
646 are beyond the scope of the present study, but are an obvious next step in the
647 nanopaleomagnetic approach.
648

649 **5. Outlook and Implications**

650 FIB-nT reveals not only the true size and shape distribution of individual
651 particles, but also the required mesoscale information at the ensemble level. The spatial
652 resolution is good enough to detect particles that span the SD to PSD range (the size
653 range of most importance in rock magnetism) and the volume of sample accessible by
654 FIB-nT approaches the volumes that can now be detected paleomagnetically using
655 SQUID microscopy (i.e. tens of microns). A long-term goal of rock magnetism is to
656 understand the collective behaviour of particle ensembles based on fundamental physical
657 principles. Some recent progress in this area has been made (Harrison and Lascu 2014),
658 but current models are still reliant on the assumption of uniaxial, single-domain
659 behaviour. The combination of FIB-nT and finite-element micromagnetics goes some
660 way towards bridging the gap between what we currently model and how samples

actually behave in the real world. We are still some way, however, from a general ensemble model that captures the intricacies of the PSD state.

Acknowledgements

The research leading to these results has received funding from the European Research Council under the European Union's Seventh Framework Programme (FP/2007-2013)/ ERC grant agreements 291522 - 3DIMAGE (P.A.M.) and 320750 – Nanopaleomagnetism (J.F.E., R.J.H., and P.A.M.). BPW and RRF were supported by NASA Emerging Worlds program grant #NNX15AH72G, the NASA Solar System Exploration and Research Virtual Institute grant #NNA14AB01A, and a generous gift from Thomas F. Peterson, Jr. The research leading to these results has received funding from the European Research Council under the European Union's Seventh Framework Programme (FP/2007-2013) / ERC Grant Agreement No. 320832- Imagine. (W.W. and P.O.C.) W.W. was also supported for this research under NERC grant NE/J020966/1- Predicting the reliability with which the geomagnetic field can be recorded in igneous rocks.

References

Almeida, T.P., Kasama, T., Muxworthy, A.R., Williams, W., Nagy, L., and Dunin-Borkowski, R.E. (2014) Observing thermomagnetic stability of nonideal magnetite particles: Good paleomagnetic recorders? Geophysical Research Letters, 41, 7041–

683 7047.
684 Almeida, T.P., Muxworthy, A.R., Kovacs, A., Williams, W., Brown, P.D., and Dunin-
685 Borkowski, R.E. (2016) Direct visualization of the thermomagnetic behavior of
686 pseudo-single-domain magnetite particles. Science Advances, 2, e1501801–
687 e1501801.
688 Bera, B., Mitra, S.K., and Vick, D. (2011) Understanding the micro structure of Berea
689 Sandstone by the simultaneous use of micro-computed tomography (micro-CT) and
690 focused ion beam-scanning electron microscopy (FIB-SEM). Micron (Oxford,
691 England : 1993), 42, 412–8.
692 Bushby, A.J., P'ng, K.M.Y., Young, R.D., Pinali, C., Knupp, C., and Quantock, A.J.
693 (2011) Imaging three-dimensional tissue architectures by focused ion beam scanning
694 electron microscopy. Nature protocols, 6, 845–58.
695 Carriero, A., Doube, M., Vogt, M., Busse, B., Zustin, J., Levchuk, A., Schneider, P.,
696 Müller, R., and Shefelbine, S.J. (2014) Altered lacunar and vascular porosity in
697 osteogenesis imperfecta mouse bone as revealed by synchrotron tomography
698 contributes to bone fragility. Bone, 61, 116–24.
699 Church, N., Feinberg, J.M., and Harrison, R. (2011) Low-temperature domain wall
700 pinning in titanomagnetite: Quantitative modeling of multidomain first-order
701 reversal curve diagrams and AC susceptibility. Geochemistry, Geophysics,
702 Geosystems, 12.
703 Connolly, H., Jones, B., and Hewins, R. (1998) The flash melting of chondrules: an
704 experimental investigation into the melting history and physical nature of chondrule
705 precursors. Geochimica Et Cosmochimica Acta, 62, 2725–2735.

706 Crewe, A. V., and Nellist, P.D. (2009) The Scanning Transmission Electron Microscope.
707 In J. Orloff, Ed., Handbook of Charged PArticle Optics pp. 497–522.
708 De Winter, D.A.M., Schneijdenberg, C.T.W.M., Lebbink, M.N., Lich, B., Verkleij, A.J.,
709 Drury, M.R., and Humbel, B.M. (2009) Tomography of insulating biological and
710 geological materials using focused ion beam (FIB) sectioning and low-kV BSE
711 imaging. Journal of microscopy, 233, 372–83.
712 Doube, M., Kłosowski, M.M., Arganda-Carreras, I., Cordelières, F.P., Dougherty, R.P.,
713 Jackson, J.S., Schmid, B., Hutchinson, J.R., and Shefelbine, S.J. (2010) BoneJ: Free
714 and extensible bone image analysis in ImageJ. Bone, 47, 1076–9.
715 Fabian, K., Kirchner, A., Williams, W., Heider, F., Leibl, T., and Huber, A. (1996)
716 Three-dimensional micromagnetic calculations for magnetite using FFT.
717 Geophysical Journal International, 124, 89–104.
718 Feinberg, J.M., Wenk, H.R., Renne, P.R., and Scott, G.R. (2004) Epitaxial relationships
719 of clinopyroxene-hosted magnetite determined using electron backscatter diffraction
720 (EBSD) technique. American Mineralogist, 89, 462–466.
721 Feinberg, J.M., Scott, G.R., Renne, P.R., and Wenk, H.-R. (2005) Exsolved magnetite
722 inclusions in silicates: Features determining their remanence behavior. Geology, 33,
723 513.
724 Flinn, D. (1962) On folding during three-dimensional progressive deformation. Quarterly
725 Journal of the Geological Society, 118, 385–428.
726 Fu, R.R., Weiss, B.P., Lima, E.A., Harrison, R.J., Bai, X.-N., Desch, S.J., Ebel, D.S.,
727 Suavet, C., Wang, H., Glenn, D., and others (2014) Solar nebula magnetic fields
728 recorded in the Semarkona meteorite. Science, 346, 1089–1092.

729 Gilbert, P. (1972) Iterative methods for the three-dimensional reconstruction of an object
730 from projections. Journal of Theoretical Biology, 36, 105–117.
731 Hargraves, R.B., Johnson, D., and Chan, C.Y. (1991) Distribution anisotropy: The cause
732 of AMS in igneous rocks? Geophysical Research Letters, 18, 2193.
733 Harrison, R.J., and Lascu, I. (2014) FORCulator: A micromagnetic tool for simulating
734 first-order reversal curve diagrams. Geochemistry, Geophysics, Geosystems, 15,
735 4671–4691.
736 Hewins, R., Connolly, H., Lofgren, G., and Libourel, G. (2005) Experimental constraints
737 on chondrule formation, 341, 286–316.
738 Holzer, L., and Cantoni, M. (2012) REVIEW OF FIBTOMOGRAPHY. In I. Utke, S.
739 Moshkalev, and P. Russell, Eds., Nanofabrication Using Focused Ion and Electron
740 Beams Principles and Applications pp. 410–435.
741 Holzer, L., Indutnyi, F., Gasser, P.H., Münch, B., and Wegmann, M. (2004) Three-
742 dimensional analysis of porous BaTiO3 ceramics using FIB nanotomography.
743 Journal of microscopy, 216, 84–95.
744 Hubert, A. (1967) Der Einfluß der Magnetostriktion auf die magnetische Bereichsstruktur
745 einachsiger Kristalle, insbesondere des Kobalts. physica status solidi (b), 22, 709–
746 727.
747 Hubert, A., and Rave, W. (1999) How well-defined are closure domains? Journal of
748 Magnetism and Magnetic Materials, 197, 325–326.
749 Hubert, A., and Schäfer, R. (1998) Magnetic Domains: The Analysis of Magnetic
750 Microstructures, 1st ed. Springer Science & Business Media.
751 Keller, L.M., Holzer, L., Wepf, R., and Gasser, P. (2011a) 3D geometry and topology of

752 pore pathways in Opalinus clay: Implications for mass transport. Applied Clay
753 Science, 52, 85–95.
754 Keller, L.M., Holzer, L., Wepf, R., Gasser, P., Münch, B., and Marschall, P. (2011b) On
755 the application of focused ion beam nanotomography in characterizing the 3D pore
756 space geometry of Opalinus clay. Physics and Chemistry of the Earth, Parts A/B/C,
757 36, 1539–1544.
758 Kirby, S.H., and Wegner, M.W. (1978) Dislocation substructure of mantle-derived
759 olivine as revealed by selective chemical etching and transmission electron
760 microscopy. Physics and Chemistry of Minerals, 3, 309–330.
761 Kruhl, J.H., Wirth, R., and Morales, L.F.G. (2013) Quartz grain boundaries as fluid
762 pathways in metamorphic rocks. Journal of Geophysical Research: Solid Earth, 118,
763 1957–1967.
764 Landrot, G., Ajo-Franklin, J.B., Yang, L., Cabrini, S., and Steefel, C.I. (2012)
765 Measurement of accessible reactive surface area in a sandstone, with application to
766 CO2 mineralization. Chemical Geology, 318-319, 113–125.
767 Lappe, S.-C.L.L., Church, N.S., Kasama, T., da Silva Fanta, A.B., Bromiley, G., Dunin-
768 Borkowski, R.E., Feinberg, J.M., Russell, S., and Harrison, R.J. (2011) Mineral
769 magnetism of dusty olivine: A credible recorder of pre-accretionary remanence.
770 Geochemistry, Geophysics, Geosystems, 12, n/a–n/a.
771 Lappe, S.-C.L.L., Feinberg, J.M., Muxworthy, A., and Harrison, R.J. (2013) Comparison
772 and calibration of nonheating paleointensity methods: A case study using dusty
773 olivine. Geochemistry, Geophysics, Geosystems, 14, 2143–2158.
774 Lee, E.W. (1955) Magnetostriction and Magnetomechanical Effects. Reports on Progress

775 in Physics, 18, 184–229.
776 Leroux, H., Libourel, G., Lemelle, L., and Guyot, F. (2003) Experimental study and TEM
777 characterization of dusty olivines in chondrites: Evidence for formation by in situ
778 reduction. Meteoritics & Planetary Science, 38, 81–94.
779 Lindquist, A.K., Feinberg, J.M., Harrison, R.J., Loudon, J.C., and Newell, A.J. (2015)
780 Domain wall pinning and dislocations: Investigating magnetite deformed under
781 conditions analogous to nature using transmission electron microscopy. Journal of
782 Geophysical Research: Solid Earth, 120, 1415–1430.
783 Muxworthy, a. R., and Williams, W. (2015) Critical single-domain grain sizes in
784 elongated iron particles: implications for meteoritic and lunar magnetism.
785 Geophysical Journal International, 202, 578–583.
786 Radeloff, C. (1964) The Determination Of The Six Magnetostriction Constants Of Iron. Z
787 Angew Phys, 17, 247–253.
788 Rave, W., Fabian, K., and Hubert, A. (1998) Magnetic states of small cubic particles with
789 uniaxial anisotropy. Journal of Magnetism and Magnetic Materials, 190, 332–348.
790 Schiffbauer, J.D., and Xiao, S. (2009) Novel application of focused ion beam electron
791 microscopy (FIB-EM) in preparation and analysis of microfossil ultrastructures: A
792 new view of complexity in early Eukaryotic organisms. PALAIOS, 24, 616–626.
793 Schindelin, J., Arganda-Carreras, I., Frise, E., Kaynig, V., Longair, M., Pietzsch, T.,
794 Preibisch, S., Rueden, C., Saalfeld, S., Schmid, B., and others (2012) Fiji: an open-
795 source platform for biological-image analysis. Nature methods, 9, 676–82.
796 Uehara, M., and Nakamura, N. (2006) Experimental constraints on magnetic stability of
797 chondrules and the paleomagnetic significance of dusty olivines. Earth and

798 Planetary Science Letters.
799 Weiss, B.P., Lima, E.A., Fong, L.E., and Baudenbacher, F.J. (2007) Paleomagnetic
800 analysis using SQUID microscopy. Journal of Geophysical Research, 112, B09105.
801 Weiss, B.P., Gattacceca, J., Stanley, S., Rochette, P., and Christensen, U.R. (2010)
802 Paleomagnetic Records of Meteorites and Early Planetesimal Differentiation. Space
803 Science Reviews, 152, 341–390.
804 Williams, D.B., and Carter, C.B. (2002) Transmission Electron Microscopy.
805 Characterization of Materials. Springer Science.
806 Williams, W., and Fabian, K. (2016) MERRILL: A finite element micromagnetic
807 modeling package for rock magnetism. In Prep.
808

809 **Figure Captions**

810

811 **Figure 1** (a) SEM micrograph of Semarkona Dusty Olivine Grain DOC5. White box
812 indicates region used for FIB-nT and S/TEM studies. (b) Top down FIB micrograph of
813 FIB-nT MROI after trenches have been milled. Hourglass structure is a fiducial mark to
814 assist in mill pattern placement. (c-e) The cyclic sequence of steps for each 20 nm slice in
815 FIB-nT volume collected.

816

817 **Figure 2 (a)** BSE SEM micrograph from slice 151 where medium grey is olivine and the
818 light grey are the Fe nanoparticles. Also visible are non-crystalline materials such as
819 charging of amorphous silica (saturated white) and holes and/or uncharged silica
820 (saturated black). (b) Binary segmented image of same BSE image after denoising and

821 manual artefact removal this leaves particles as white voxels and all other materials as
822 black.
823
824 **Figure 3** Transformation of tomographic particle voxels into tetrahedral meshes for FEM
825 modelling for particle number 8, the smallest prolate particle captured in the FIB-nT
826 volume. (a) Initially the individual particles form a rough box like volume, described by
827 the voxels of the original FIB-nT volume. (b) By fitting a bounding polyhedron subject to
828 the Poisson equation, a rough triangular surface mesh is generated. (c) Applying a
829 smoothing filter to the Poisson surface results in a mesh with triangular nodes spaced
830 every < 2.5 nm. This is too high a mesh density for efficient micromagnetic modelling.
831 (c) Using a Delaunay triangulation function, the surface mesh is coarsened to the desired
832 5 nm-resolution triangular surface mesh. This surface is then used to seed the interior
833 tetrahedral elements of the same size.
834
835 **Figure 4** Orthogonal views of the reconstructed volume on the (a) X-Y plane, (b) X-Z
836 plane and (c) Y-Z plane. (d) Close up detail of several larger particles where faceting is
837 observable.
838
839 **Figure 5** Histograms of best-fitting ellipsoid diameters for the (a) major, (b) intermediate
840 and (c) minor axes of each Fe particle in the FIB-nT reconstruction.
841
842 **Figure 6 (a)** Flinn plot of the particle aspect ratios. The 45° line describes particles with a
843 Flinn ratio of 1. The particle aspect ratios are plotted with colour and point size scaling as

844 a function of the major radius length in nanometres. (b) Histogram of Flinn ratios (<1 for
845 oblate, > 1 for prolate) from the FIB-nT volume.
846
847 **Figure 7** Stereographic projection showing the orientation of major (red circles),
848 intermediate (green circles) and minor (blue circles) axes of the best-fitting ellipsoids.
849 Open circles are upper hemisphere, closed circles are lower hemisphere. The three solid
850 triangles plot the measured the anisotropy of ARM susceptibility for the entire dusty
851 olivine grain studied (Maximum susceptibility is red, intermediate is green and minor is
852 blue).
853
854 **Figure 8** STEM bright field montage showing Fe particles (dark), olivine (grey) and
855 silica blebs (bright). Sub-grains are visible as small changes in grey scale in the olivine
856 host. Blue inset shows a bright-field TEM image of the highlighted Fe nanoparticle.
857 Faceting parallel to sub-grain boundaries, defined by multiple dislocations, can be
858 observed. Red inset: upper left panel shows bright-field TEM of the two highlighted Fe
859 nanoparticles; upper right panel shows the diffraction pattern of olivine matrix collected
860 at an α ftilt of -3.5° and a β -tilt of -1.1°; lower left panel shows the diffraction pattern
861 for the smaller Fe particle; lower right panel shows the STEM tomographic
862 reconstruction of the smaller Fe nanoparticle.
863
864 **Figure 9** The four types of pseudo-single domain state observed in the FEM simulations.
865 Colorbar for arrows shows the direction and magnitude of the normalized M_z component
866 of the particle magnetization. Green isosurfaces are selected to highlight the magnitude of

867 the vorticity of the moment vector field. These vary particle to particle and are selected to
868 present the minimum continuous surface. (a) Type I: single vortex with core oriented
869 parallel to the minor axis of the best-fitting ellipsoid for particle 155. (b) Type II: single
870 vortex with core oriented within the plane defined by the minor and major axes of the
871 best-fitting ellipsoid for particle 165. (c) Type III: single vortex with core oriented
872 parallel to the major axis of the best-fitting ellipsoid for particle 75. (d) Type IV: multiple
873 core/wall-like structures for particle 233 with the magnetic field applied along the Y and
874 Z-axis respectively.
875
876 **Figure 10** Evolution of vortex core morphology. (a) The vortex core of particle 48
877 plotted for a helicity level of 180. (b) The vortex core of particle 165 plotted for a helicity
878 level of 40. (c) The vortex core of particle 8 plotted for a helicity level of 80. (d) The
879 vortex core of particle 75 plotted for a helicity level of 75.
880
881 **Figure 11** Thresholded anisotropy energy surfaces for particle 233, showing wall regions
882 corresponding to the highest magnetocrystalline anisotropy energy. The color of each
883 surface represents the projection of wall magnetization along the minor axis of the best-
884 fitting ellipsoid (~ parallel to X). Red is positive, blue is negative. (a) Type III remanence
885 state resulting from magnetic field applied along the X-axis. Dashed green line shows
886 approximate position of cross-section in (c). (b) Type IVa remanence state resulting from
887 magnetic field applied along the Y-axis. (c) Cross section through the anisotropy surface
888 in (a). (d) Type IVb remanence state displaying well-defined 90° walls resulting from
889 magnetic field applied along the Z-axis.

890

891 **Figure 12** (a) Schematic drawing depicting the four possible combinations of bulk spin
892 rotation and vortex core direction. (b-e) Stereograms showing the remanence vectors
893 obtained after applying fields along X (black circle), Y (black square) and Z (black
894 triangle). Diamonds show the orientation of major (red), intermediate (green) and minor
895 (blue) axes of the best-fitting ellipsoid. Lines show the traces of planes normal to the
896 corresponding axes of the best-fitting ellipsoid. Closed symbols and solid lines are lower
897 hemisphere; open symbols and dashed lines are upper hemisphere. Results are shown for
898 two Type I particles (b, c); (d) a Type II particle; and (e) a type III particle. Note also that
899 the remanence states obtained for this particle after applying a saturating fields along X
900 and Z are identical (only the X state is plotted in Fig. 12b).

901

902 **Figure 13** Calculated components of magnetization parallel to X (blue), Y (green) and Z
903 (red) as a function of applied field for the upper (solid) and lower (dashed) branches of
904 the major hysteresis loop. (a) Type I particle (364) with field applied along X. (b) Type I
905 particle (48) with field applied along Y. (c) Type I particle (48) with field applied along
906 Z. (d) Type III particle (233) with field applied along X.

907

908 **Figure 14** Thresholded anisotropy energy surface for particle 155, showing wall regions
909 corresponding to the highest magnetocrystalline anisotropy energy. The color of each
910 surface represents the projection of wall magnetization along the minor axis of the best-
911 fitting ellipsoid (~ parallel to X). Red is positive, blue is negative. Note the larger size of
912 the right hand domain (red) compared to the left hand domain (blue) is due to the

913 different size of the corresponding surface facets, and leads to a net contribution to the
914 remanence of the particle from the bulk spins.
915

916

917 **Tables**

Particle ID	Major radius (nm)	Inter. radius (nm)	Minor radius (nm)	Flinn Ratio	Mesh Vol. (nm^3)	M_{rs}/M_s X Y Z	H_c (mT) X Y Z	Rel. M_r	Min. Irrev. Field (mT)	Domain state
STEM	119	117	98	0.85	5.72E +06	0.0086 0.0086 0.0086	0.2 0.5 7	6 6 6	270 330 260	II II II
48	36	35	23	0.68	1.43E +05	0.066 0.065 -0.067	42 19 -20	1.16 1.14 1.16	260 310 300	I I I
321	54	44	28	0.78	2.97E +05	0.032 0.036 -0.032	27 2.1 -4.4	1.15 1.32 1.15	380 260 410	I I I
364	34	26	16	0.8	2.46E +05	0.042 -0.03 -0.042	37 -5 -4	1.27 0.9 1.27	290 300 >1000	I I I
8	138	79	54	1.2	2.24E +06	0.012 0.022 0.022	11 8 5	3.1 6.1 6.1	440 260 240	III III III
233	536	163	71	1.43	2.27E +07	0.013 0.016 0.0035	8 4 0.5	36.7 44.8 9.7	230 60 100	III IVa IVb
75	259	133	84	1.23	1.13E +07	0.0059 0.016 0.018	6 4 6	8.1 21.7 25.8	430 260 40	III III IVa
165	262	228	151	0.76	3.73E +07	0.0027 0.0035 0.0035	2.5 0.64 0.04	12.2 16 16	250 330 490	II II II
155	213	198	73	0.4	1.33E +07	0.004 -0.003 0.004	3.6 -0.09 1.1	7 5.6 7	500 260 300	I I I

918
919

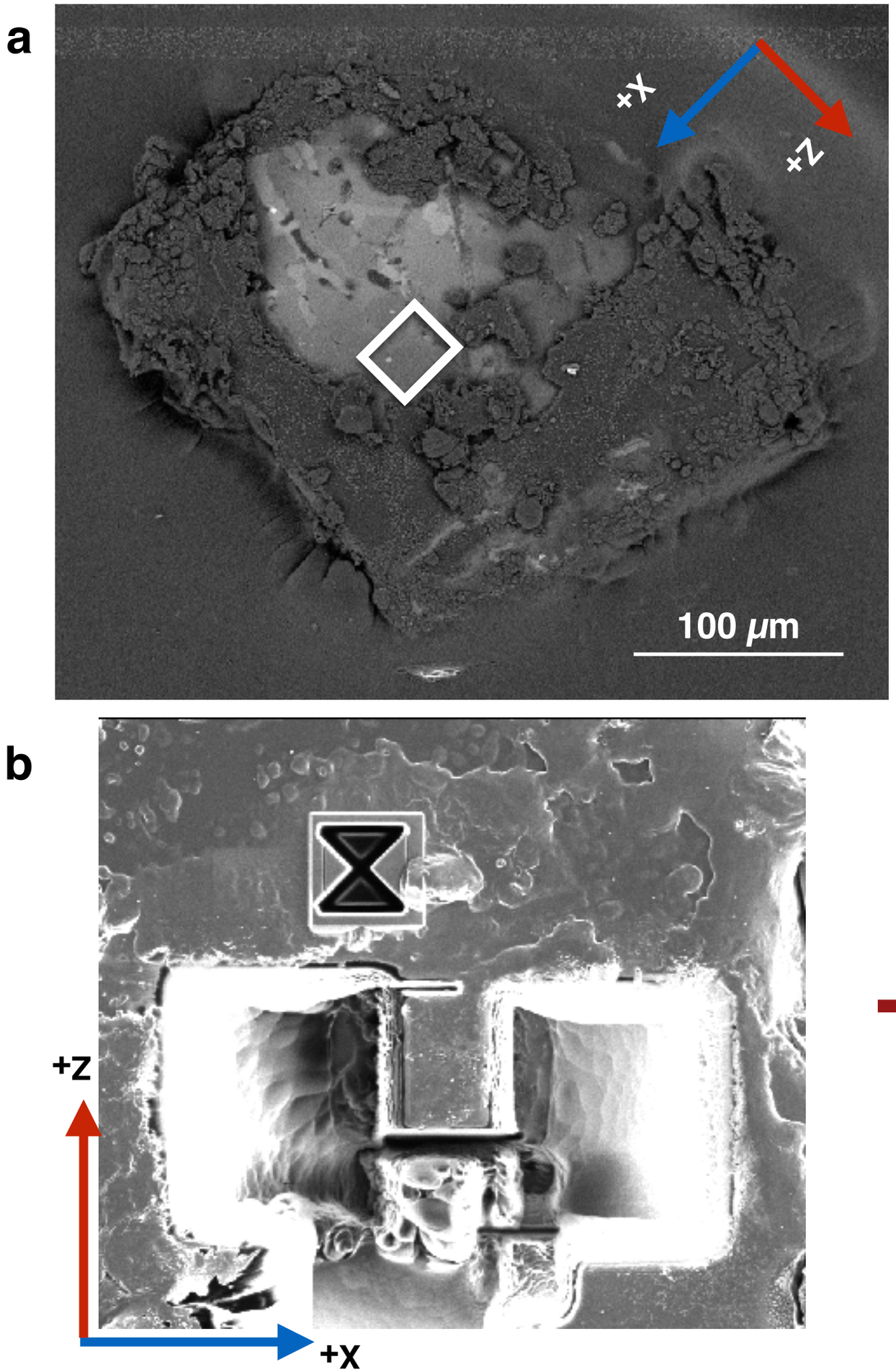

Figure 1

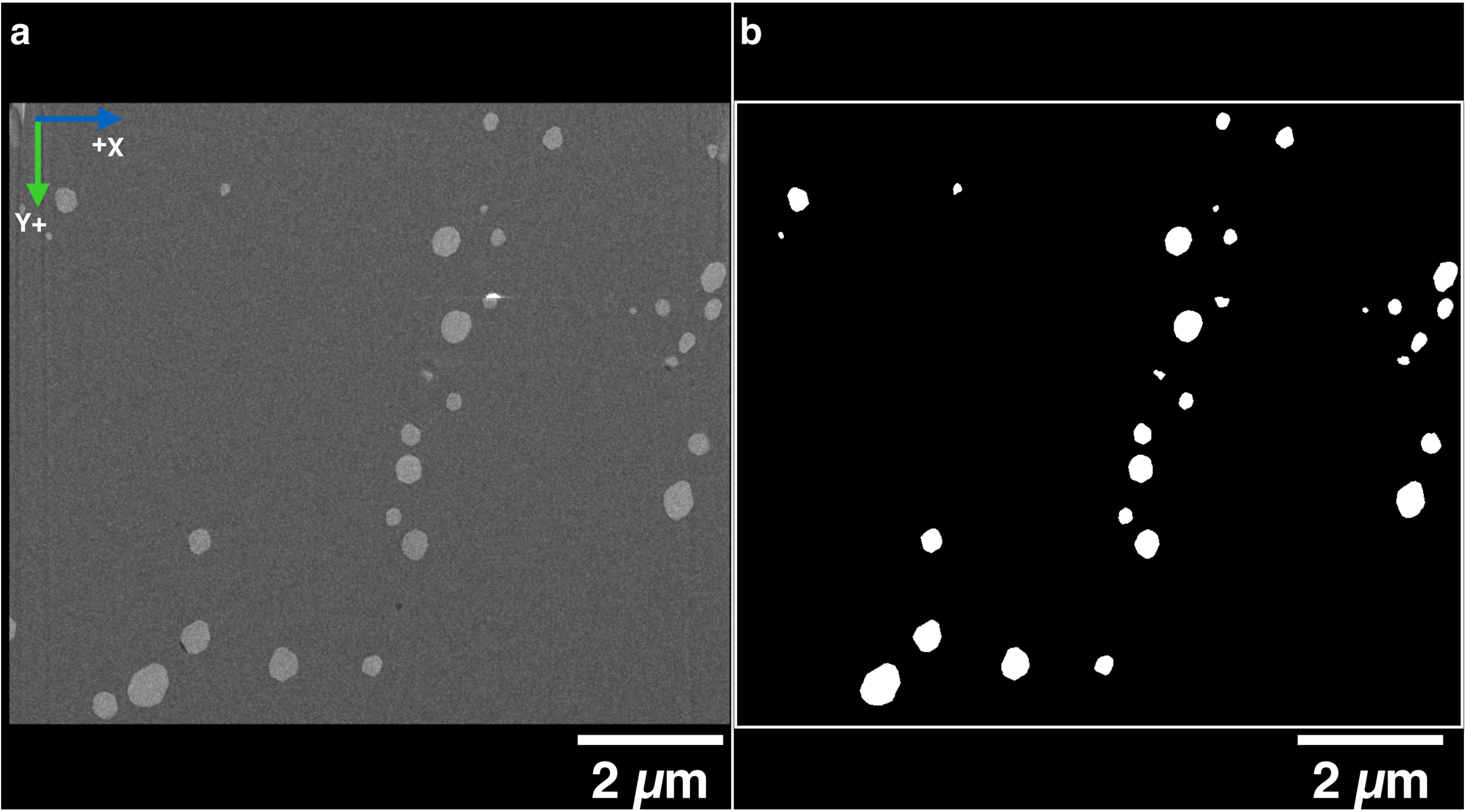

Figure 2

Figure 3

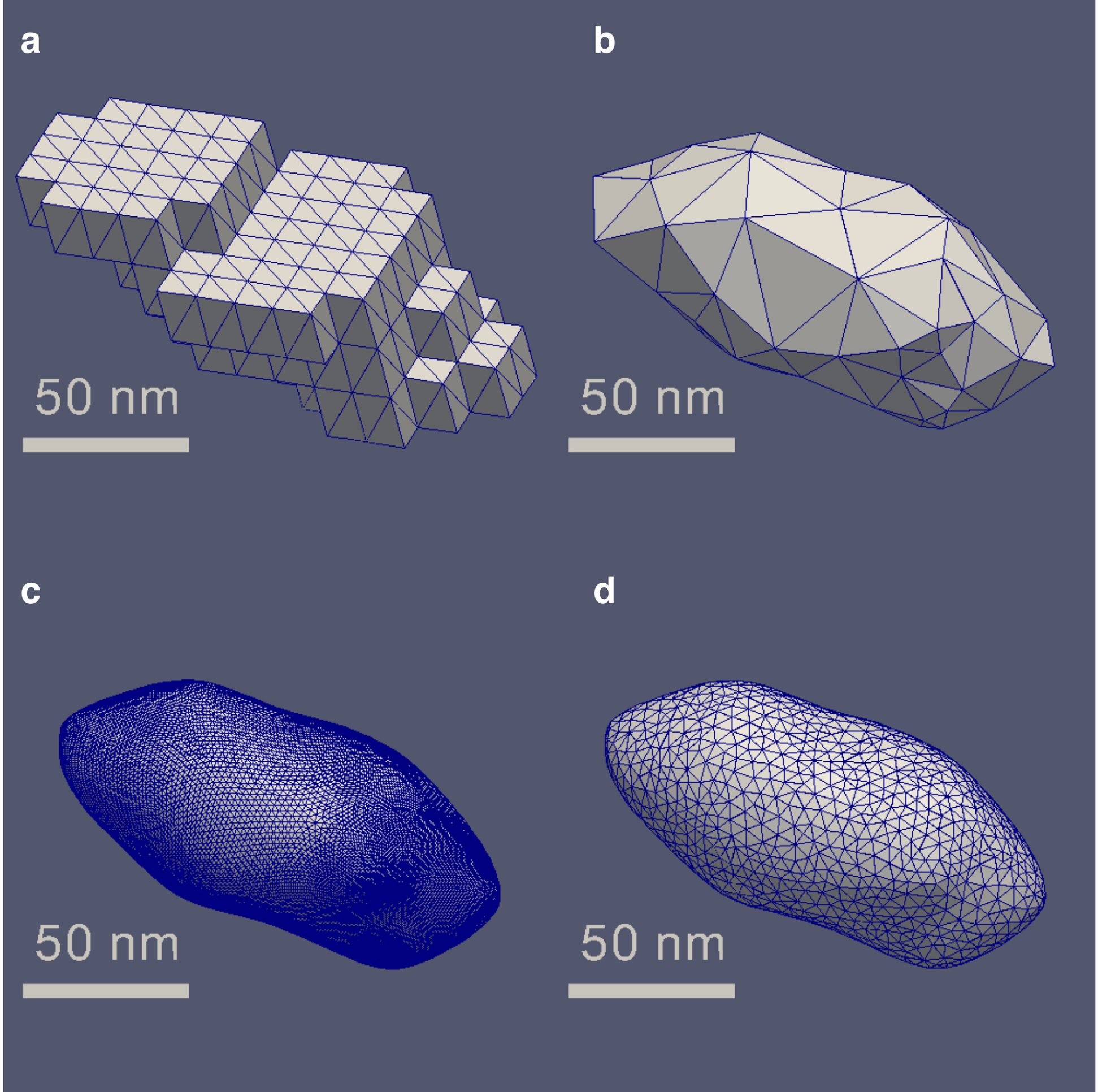

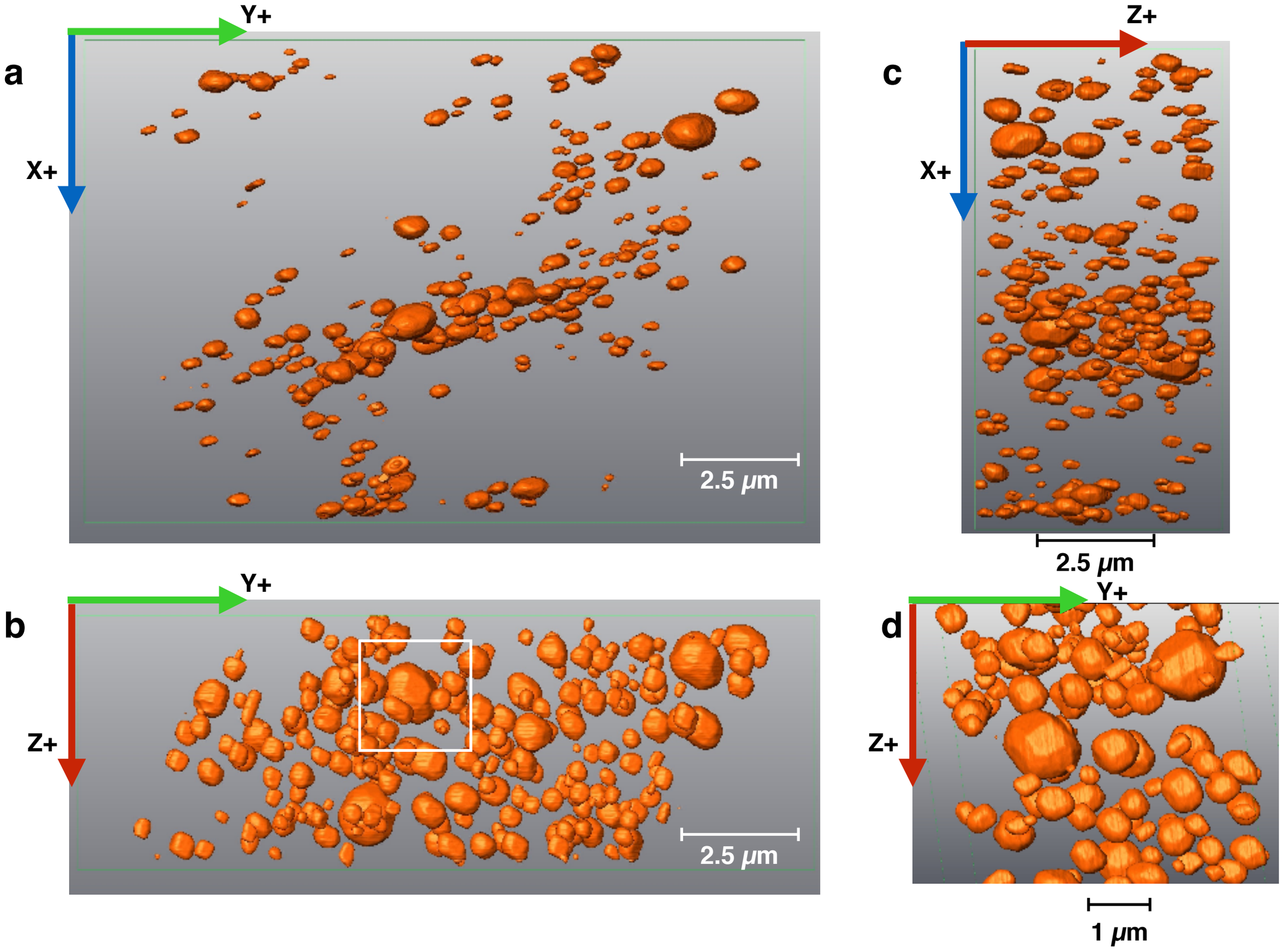

Figure 4

Figure 5

a

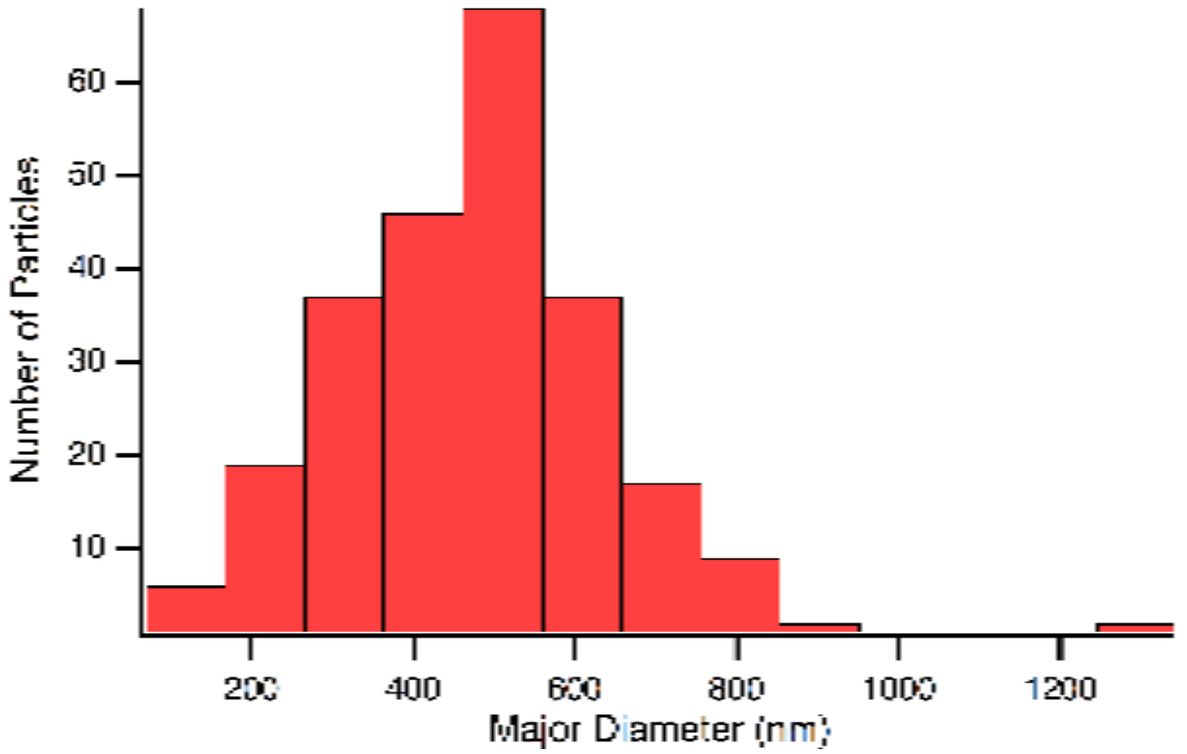
Number of Particles
60
50
40
30
20
10
200
400
600
800
1000
1200
Major Diameter (nm)

b

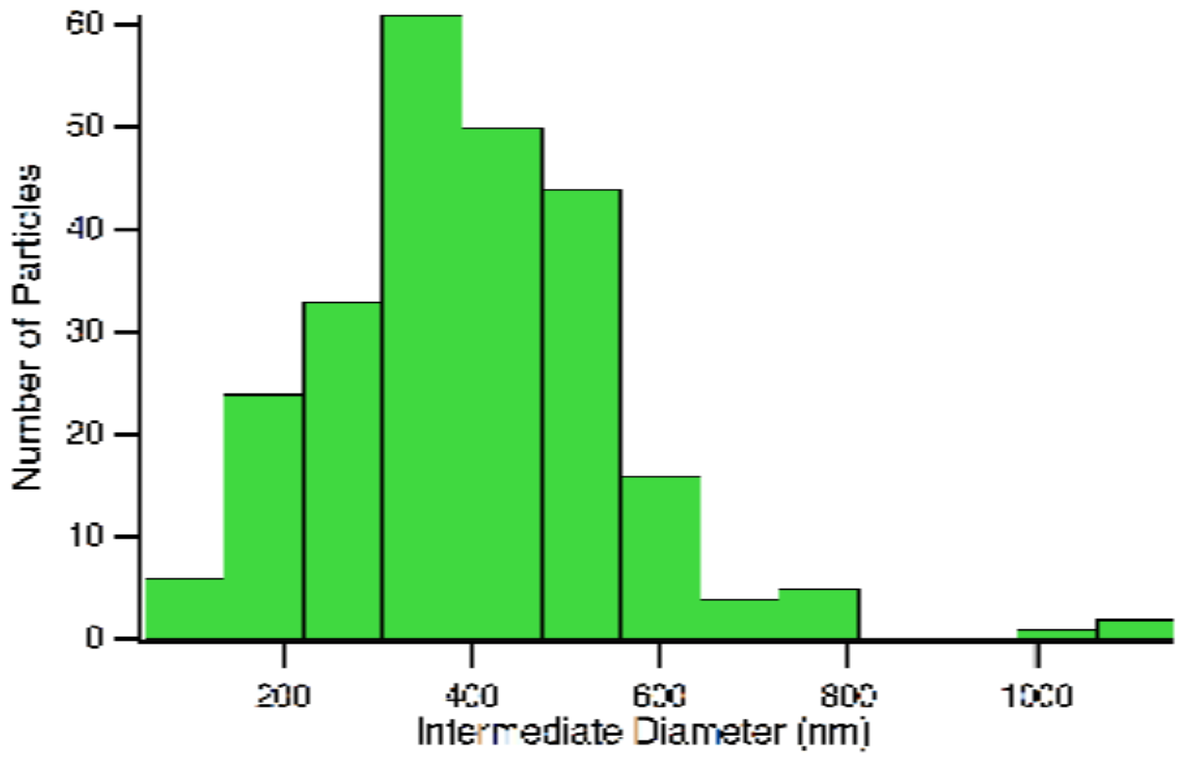
Number of Particles
60
50
40
30
20
10
0
200
400
600
800
1000
Intermediate Diameter (nm)

c

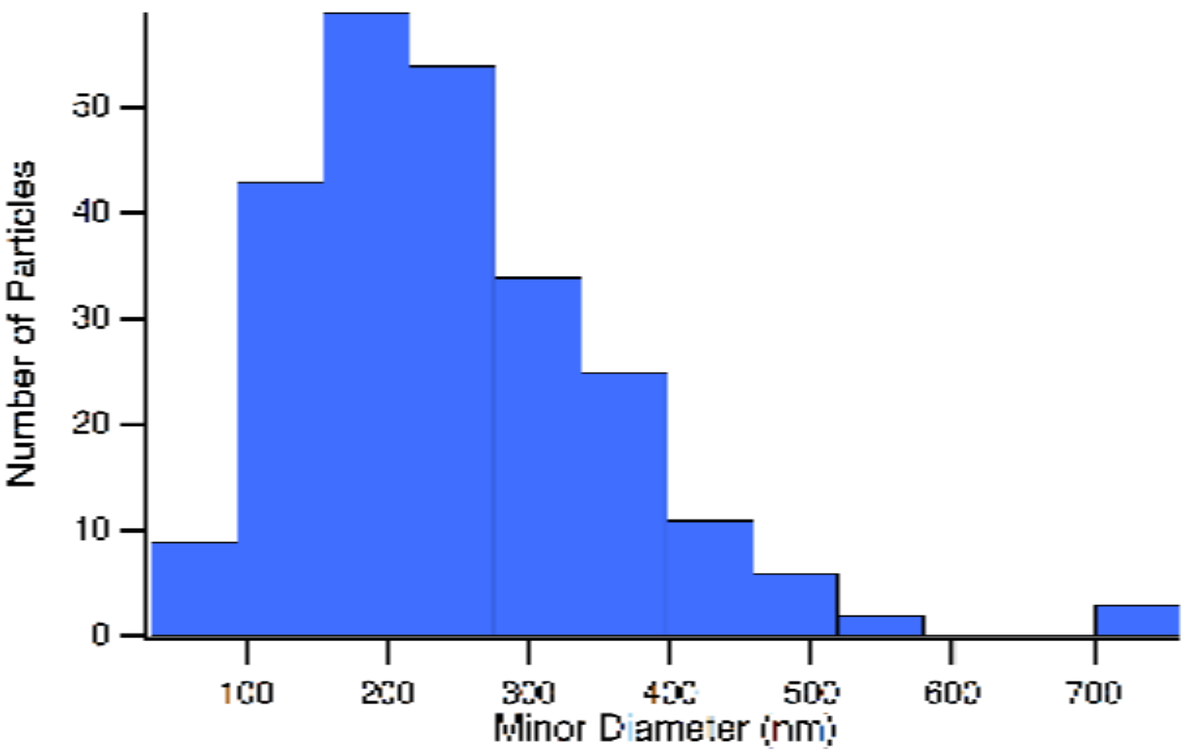
Number of Particles
50
40
30
20
10
0
100
200
300
400
500
600
700
Minor Diameter (nm)

Figure 6

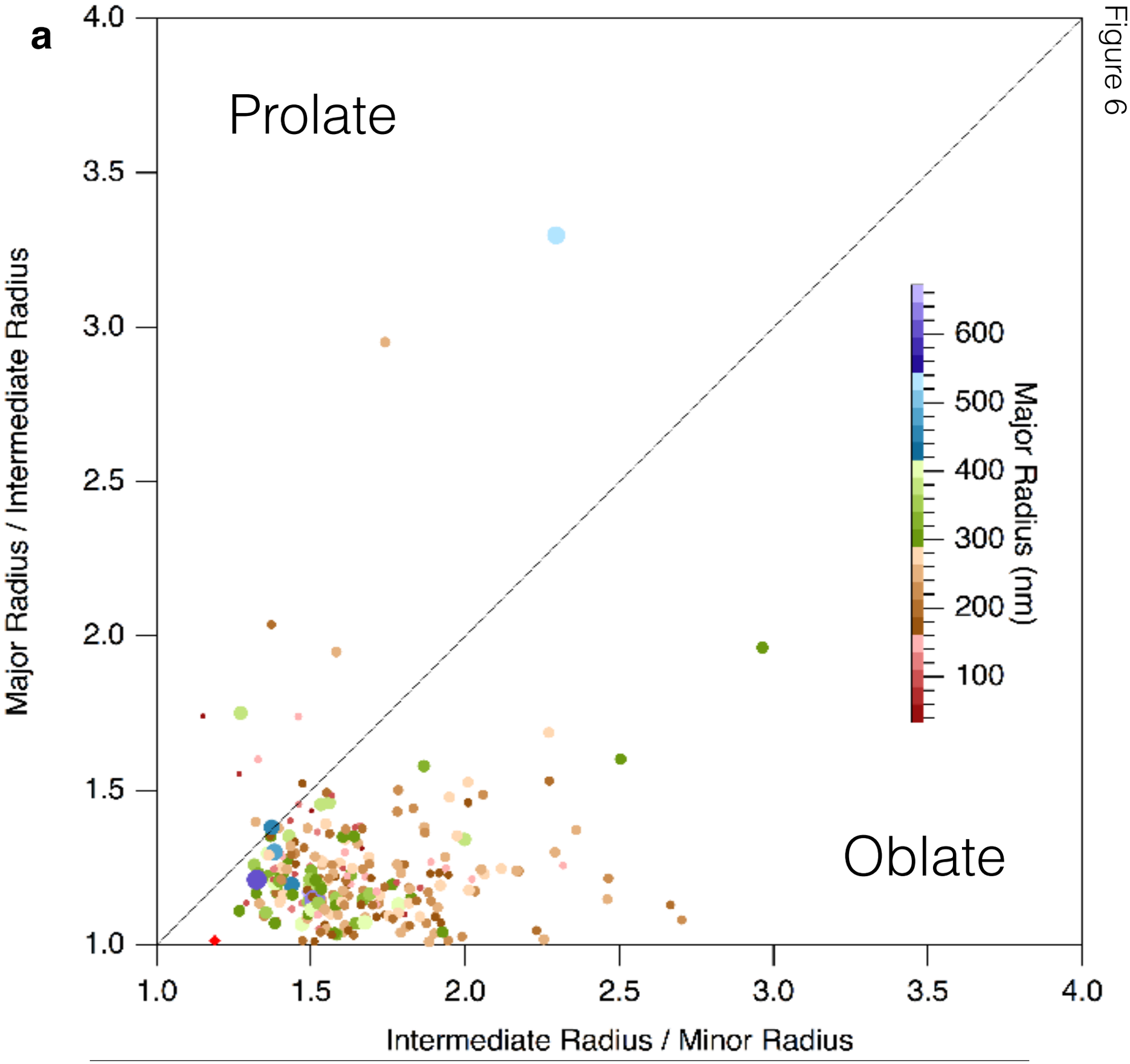
a
Prolate
Oblate
Major Radius / Intermediate Radius
Intermediate Radius / Minor Radius
Major Radius (nm)
4.0
3.5
3.0
2.5
2.0
1.5
1.0
600
500
400
300
200
100

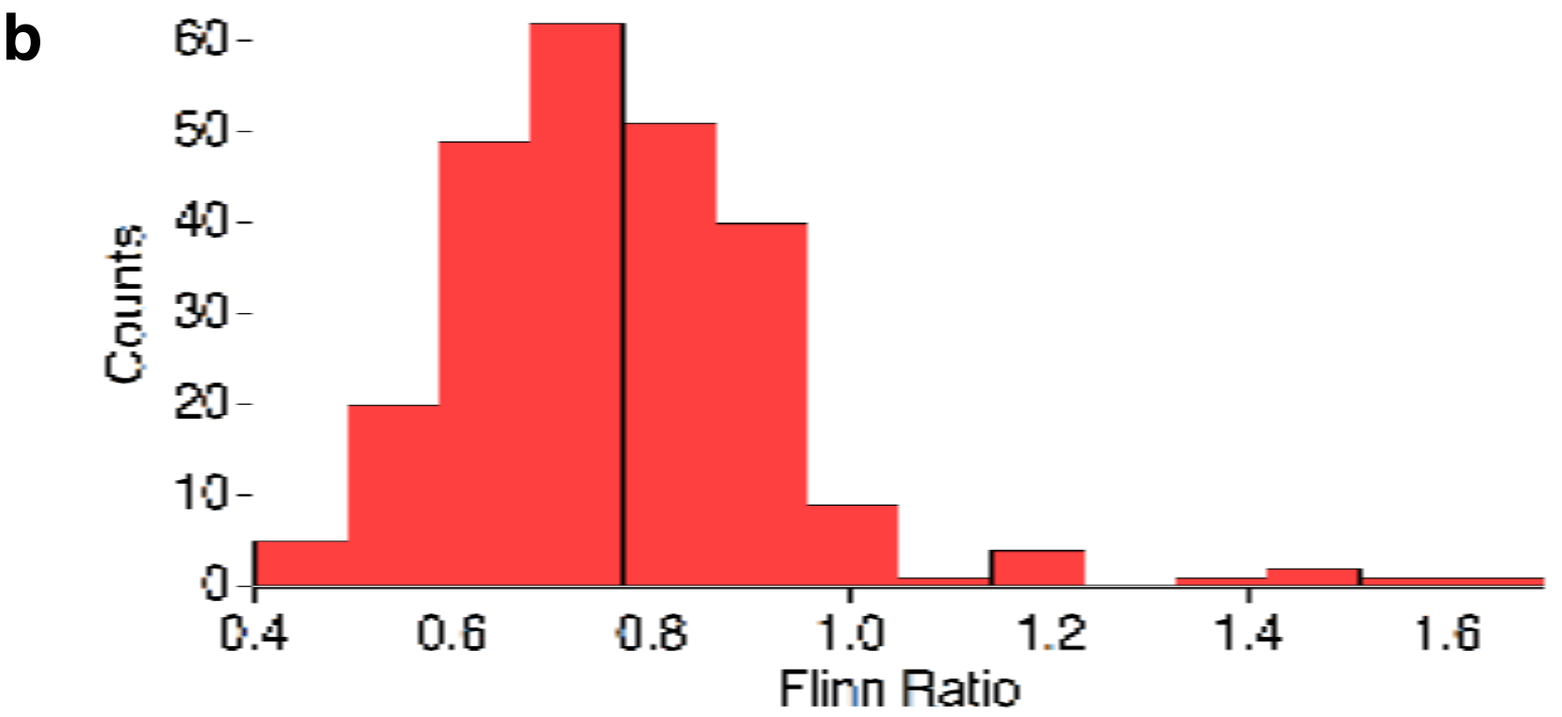
b
Counts
Flinn Ratio
60
50
40
30
20
10
0
0.4
0.6
0.8
1.0
1.2
1.4
1.6

Figure 7

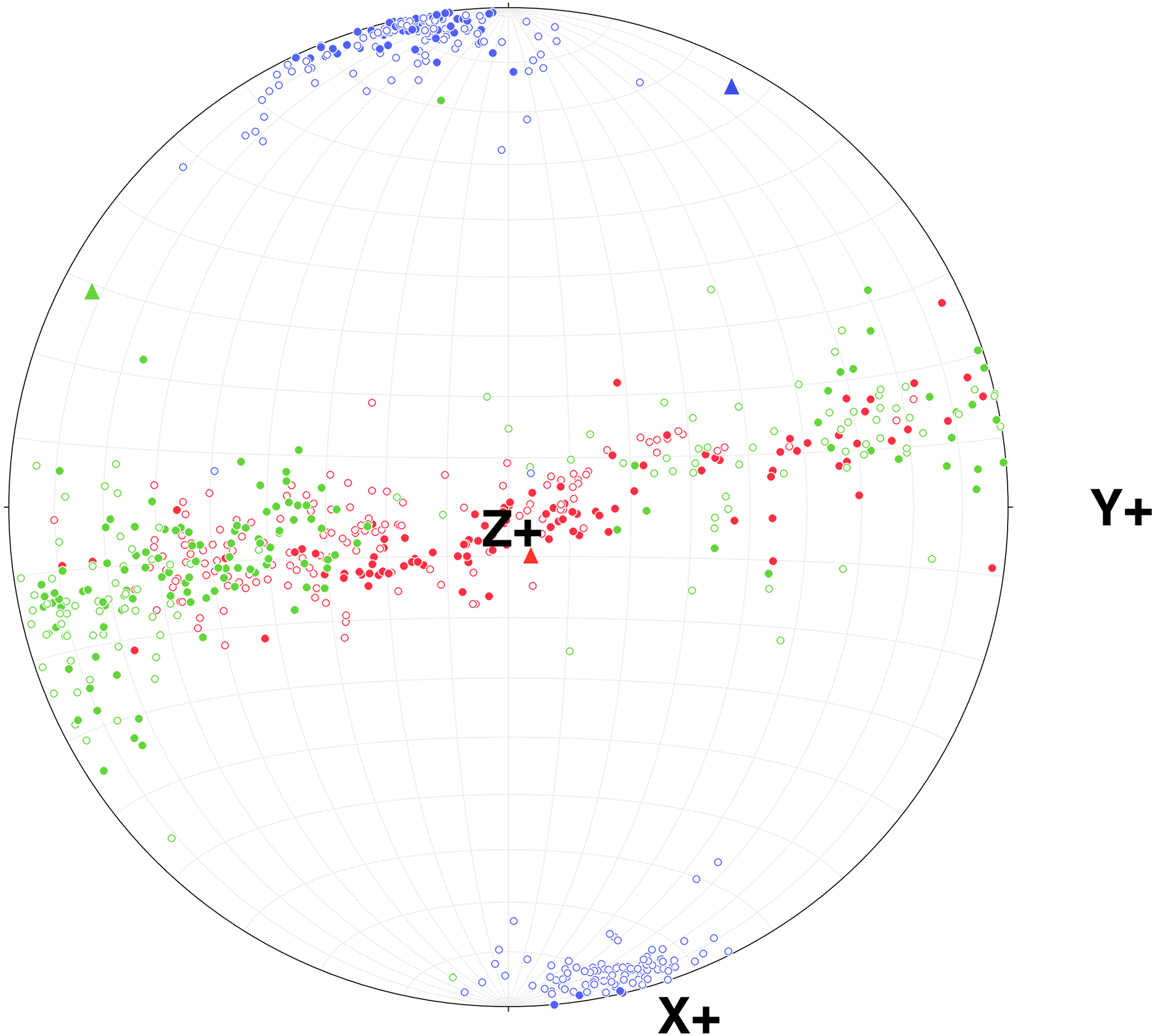

Figure 8

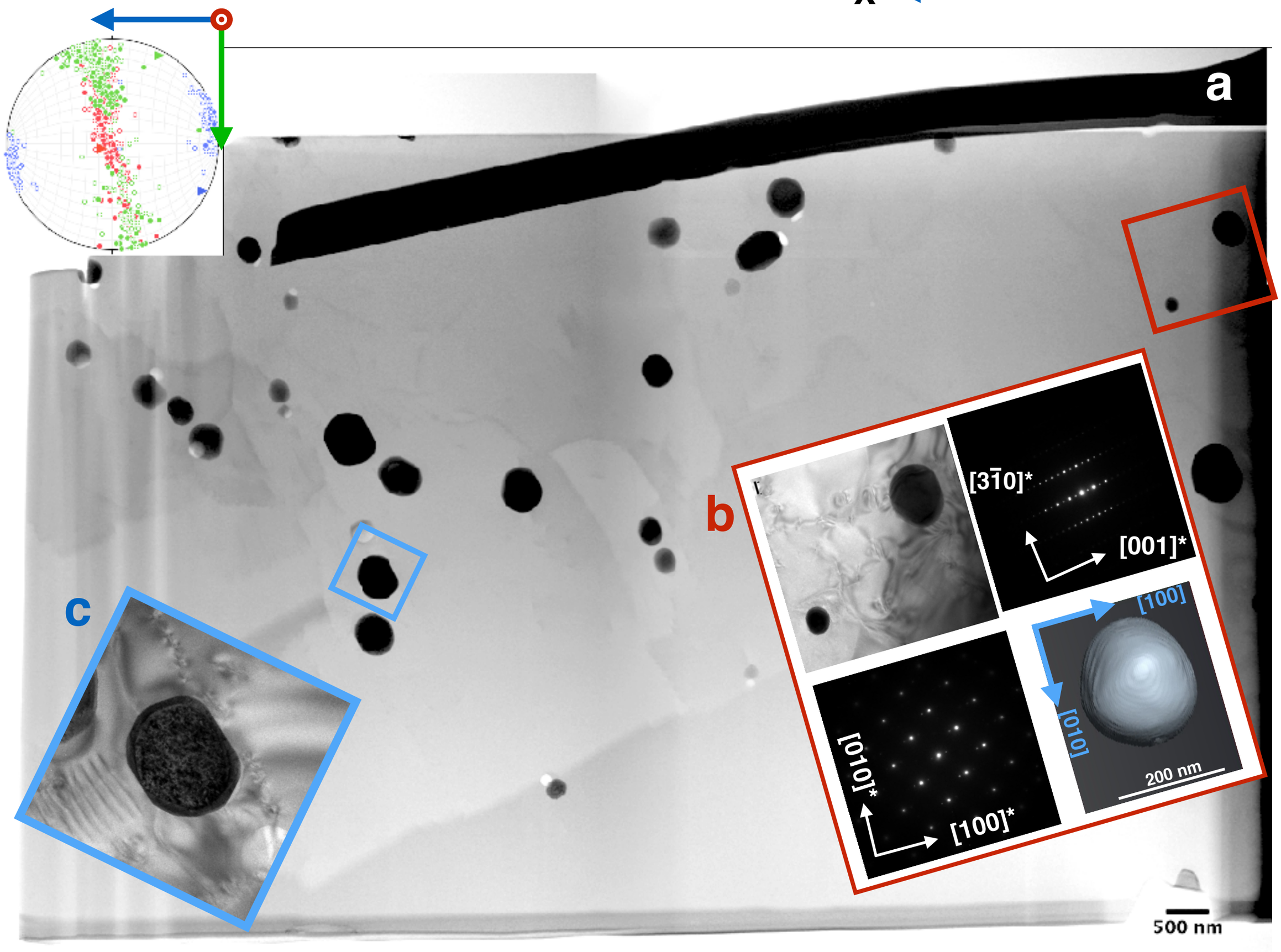

Figure 9

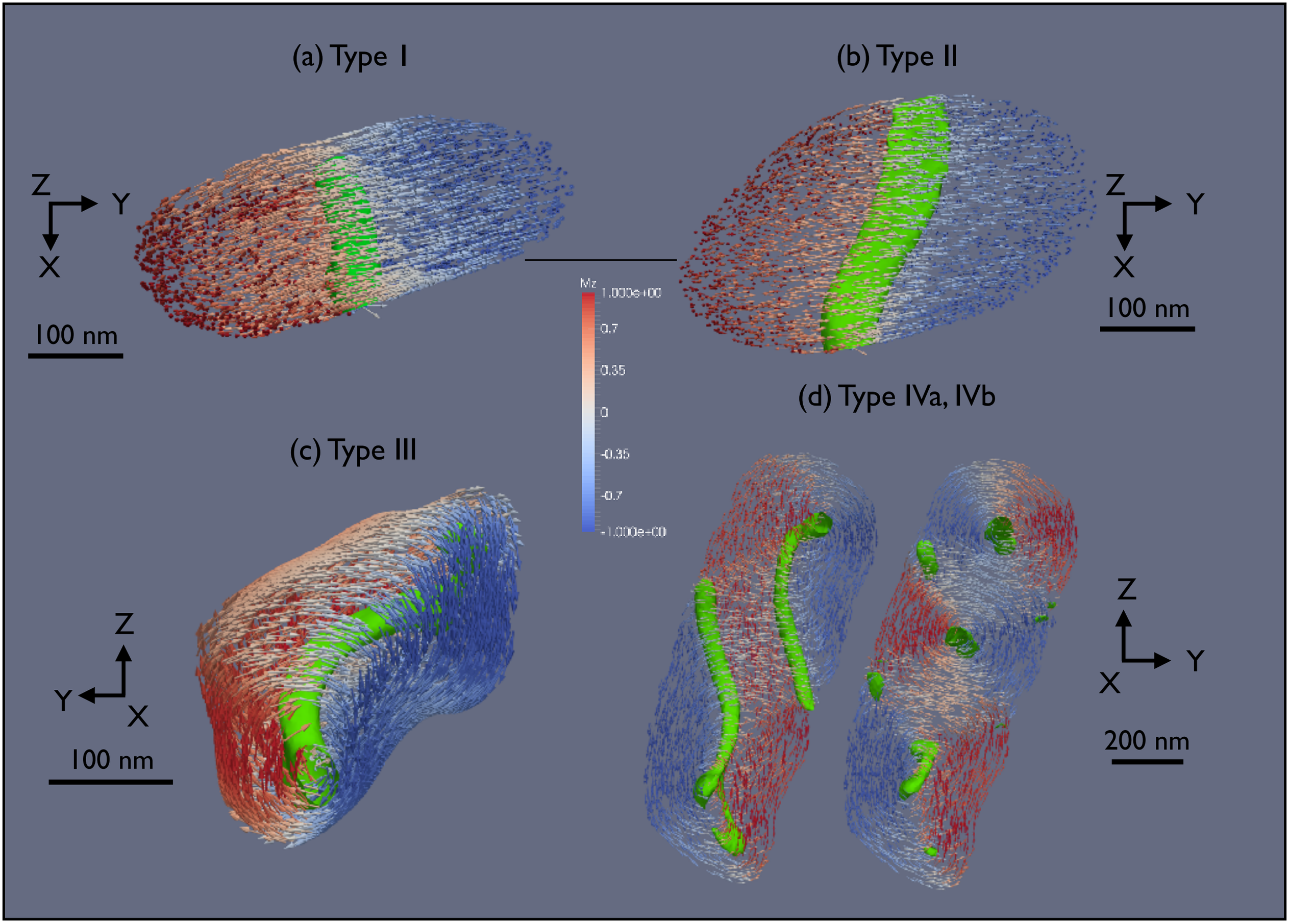
(a) Type I
Z
Y
X
100 nm
(b) Type II
Z
Y
X
100 nm
Mz
1.0000e+00
0.7
0.35
0
-0.35
-0.7
-1.0000e+00
(c) Type III
Z
Y
X
100 nm
(d) Type IVa, IVb
Z
Y
X
200 nm

Figure 10

(a) Particle 48

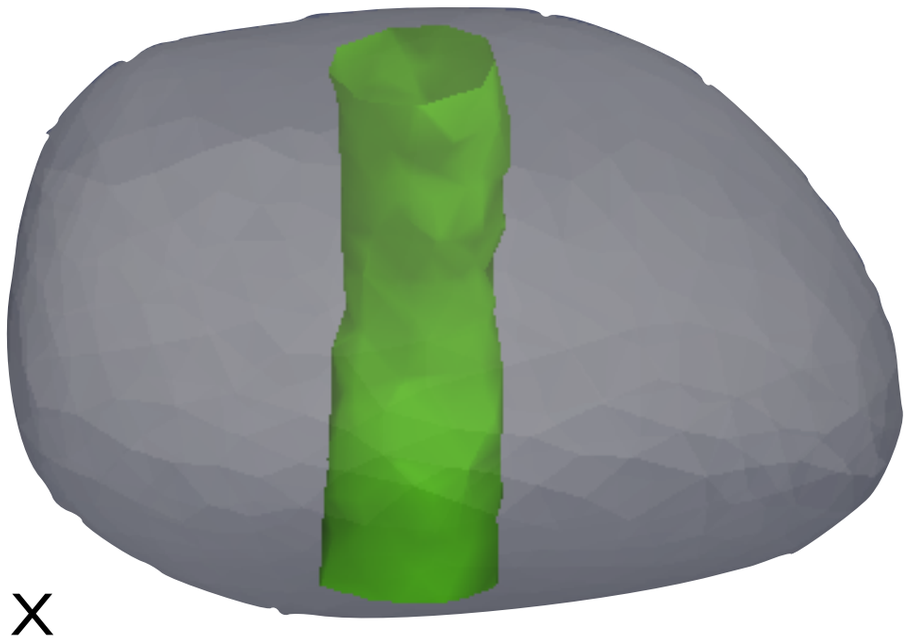

(b) Particle 165

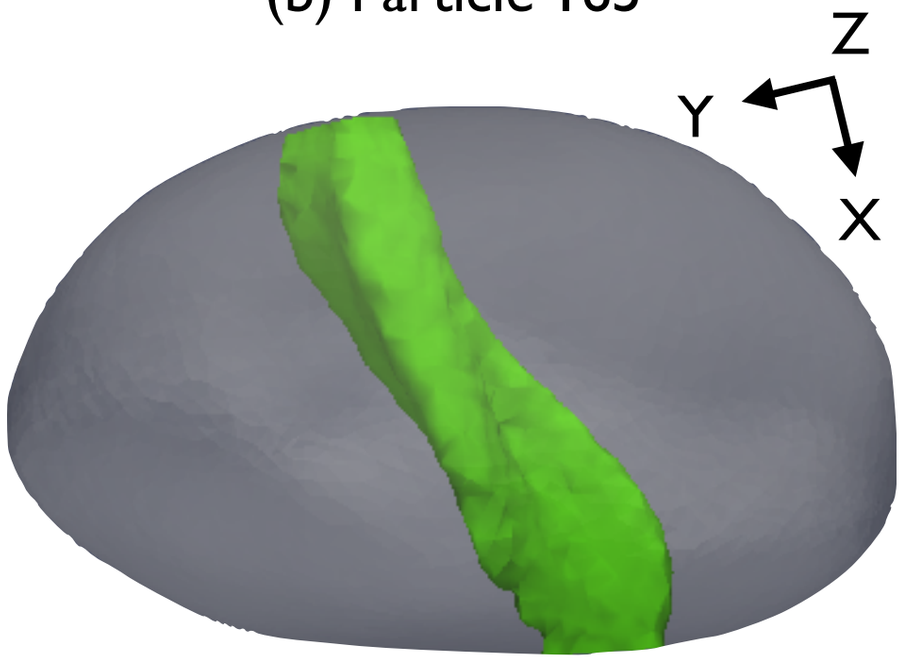

(c) Particle 8

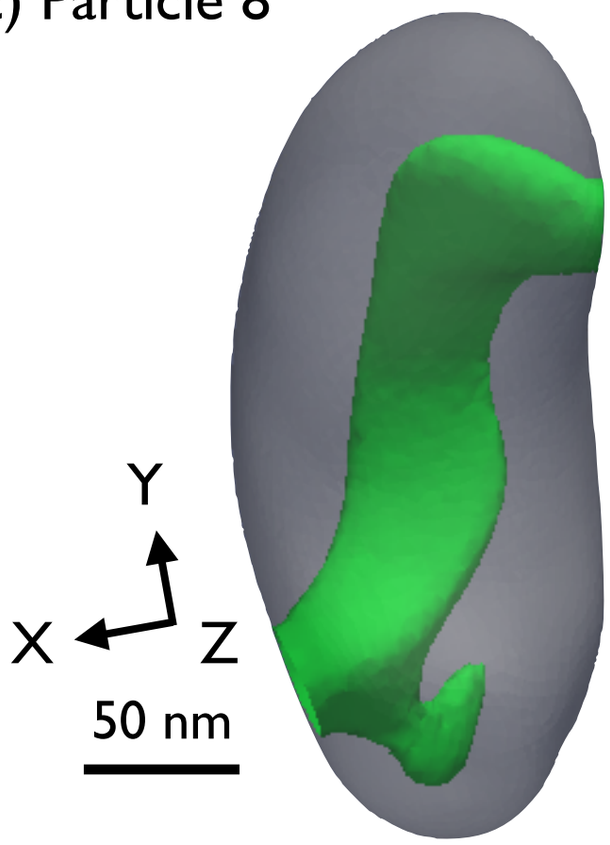

(d) Particle 75

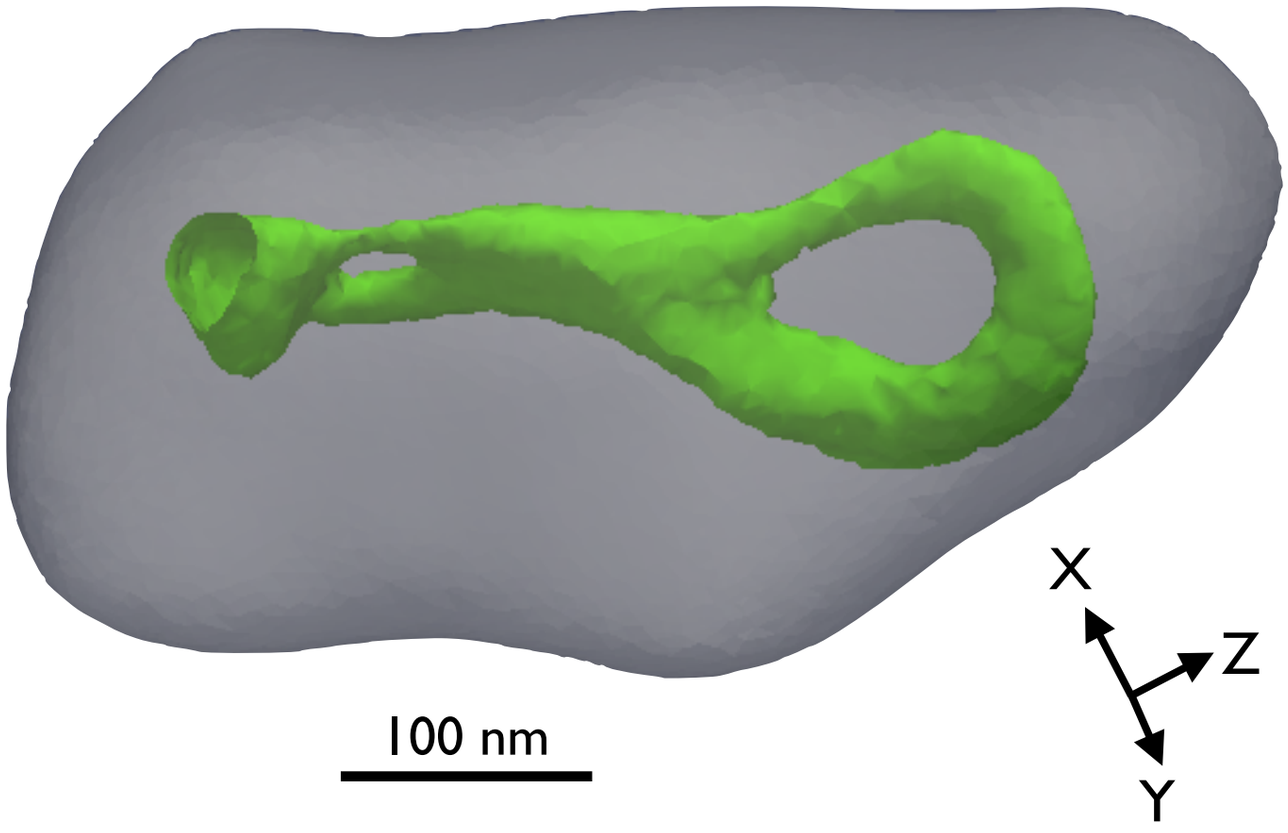

Figure 11

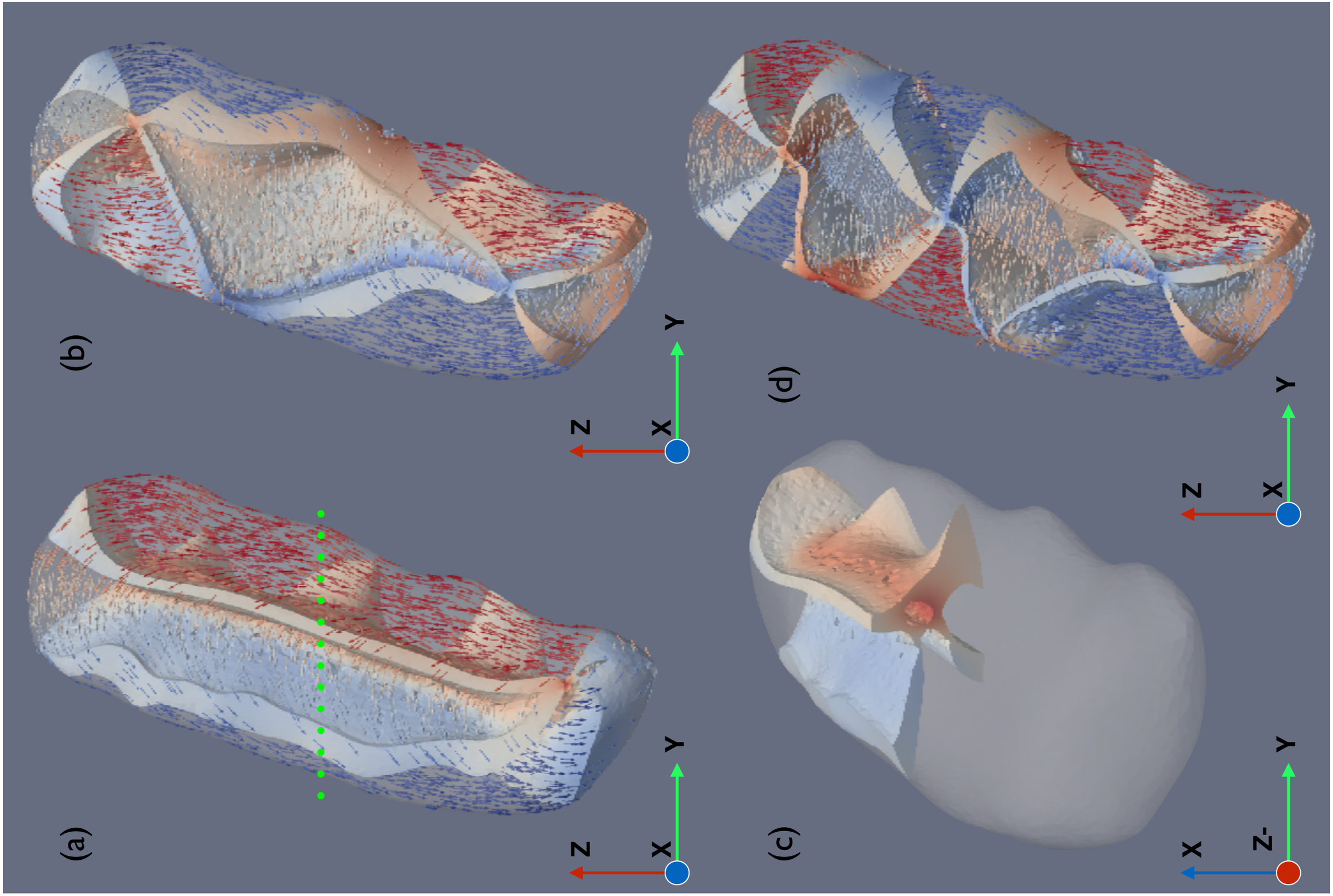

(a)

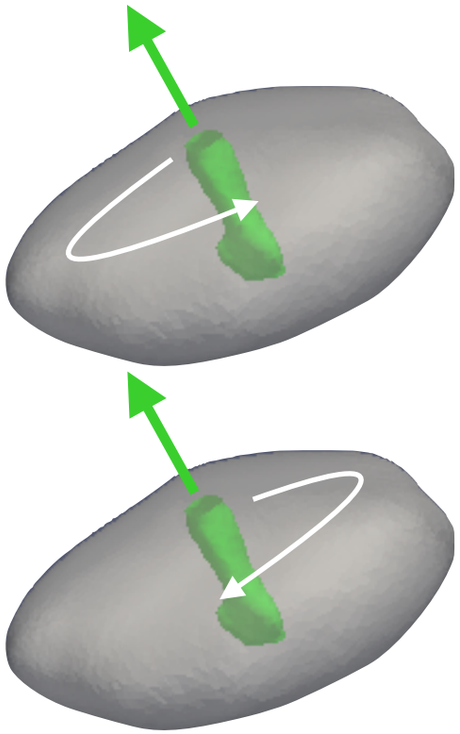

(b) Particle 364

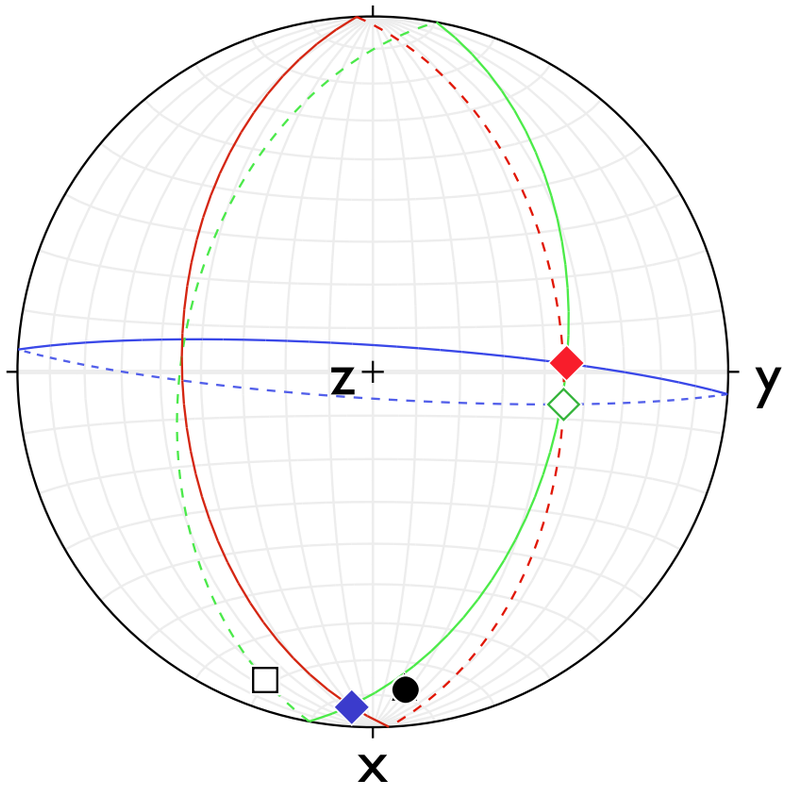

(c) Particle 155

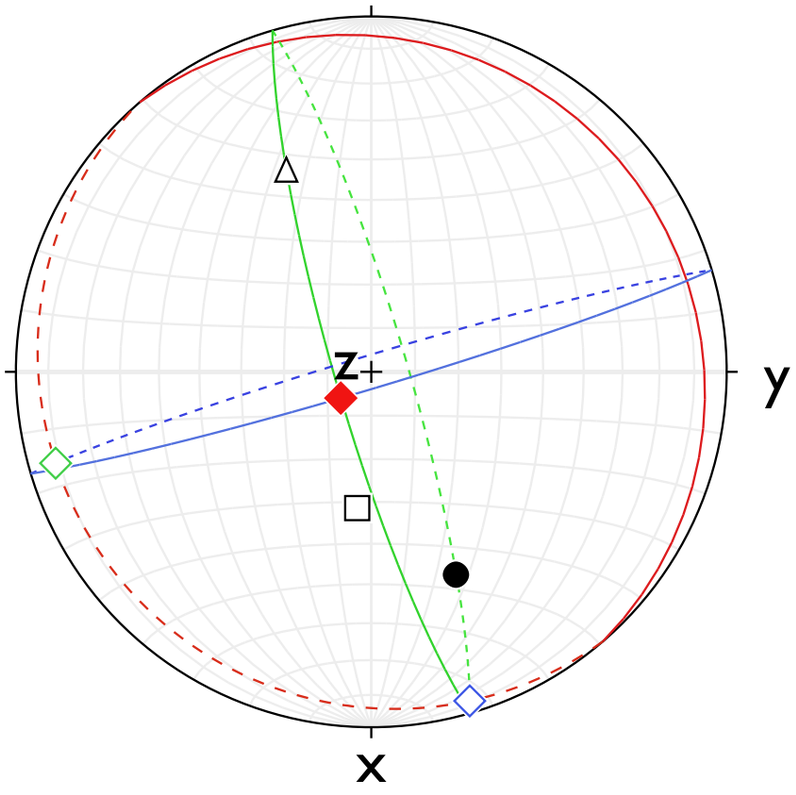

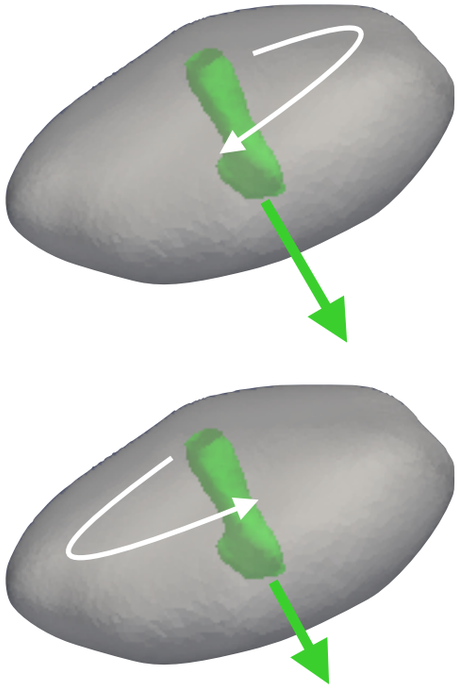

(d) Particle 165

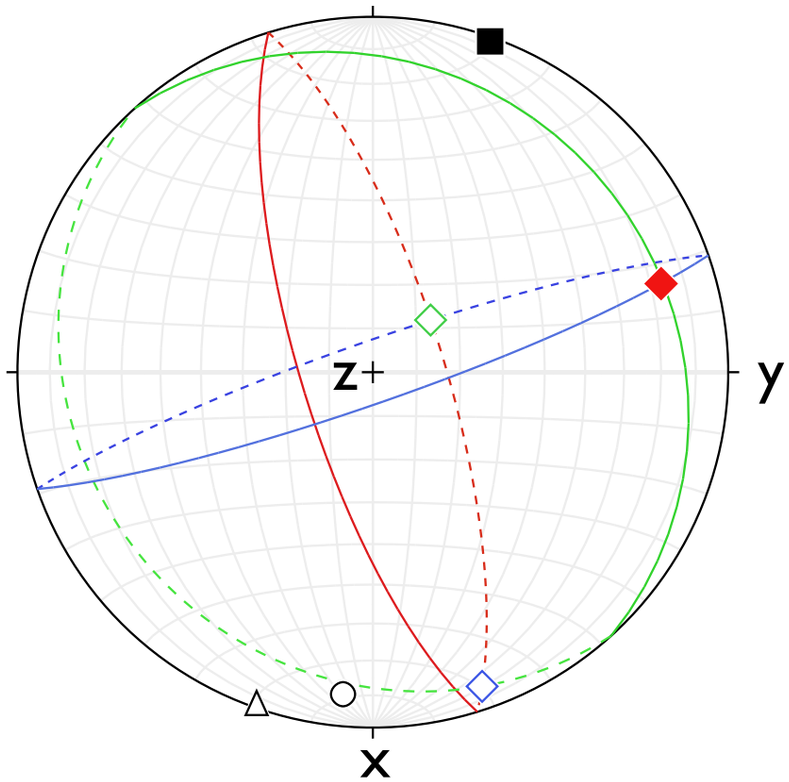

(e) Particle 8

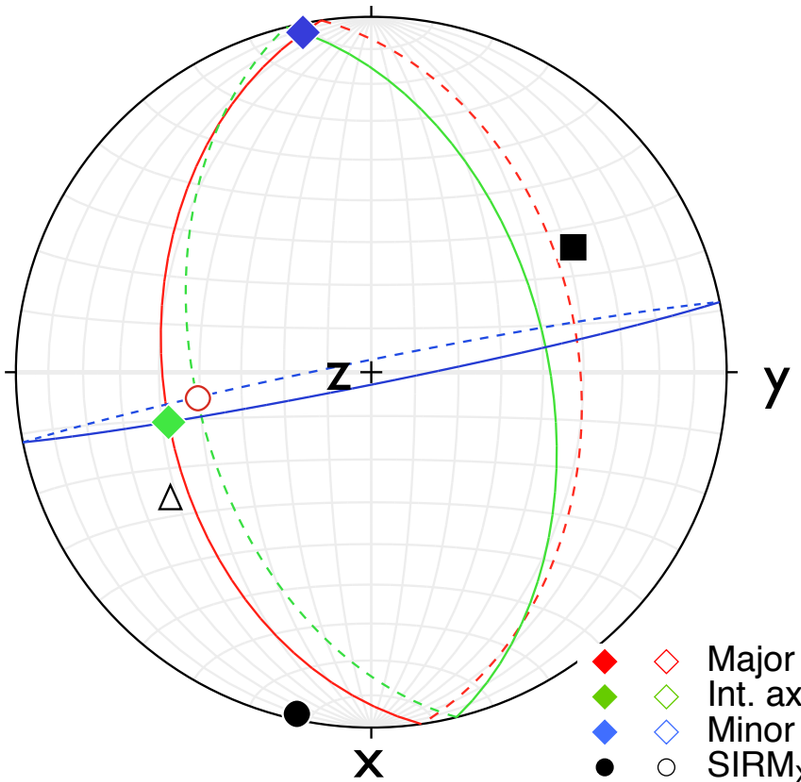

Major axis (down, up)
Int. axis (down, up)
Minor axis (down, up)
$SIRM_X$ (down, up)
$SIRM_Y$ (down, up)
$SIRM_Z$ (down, up)

Figure 12

Figure 13

(a) Particle 364 // X

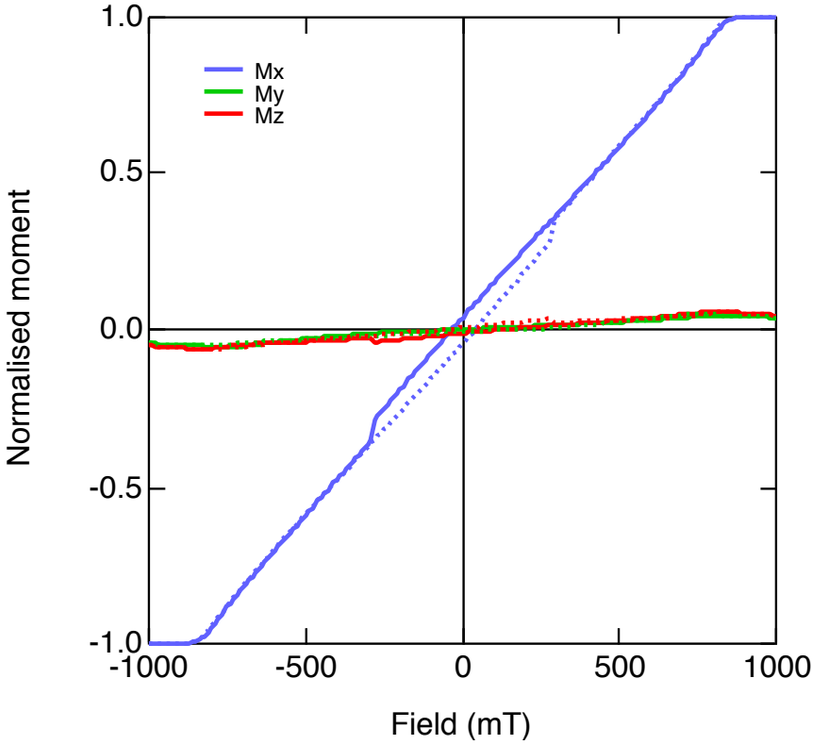

(b) Particle 48 // Y

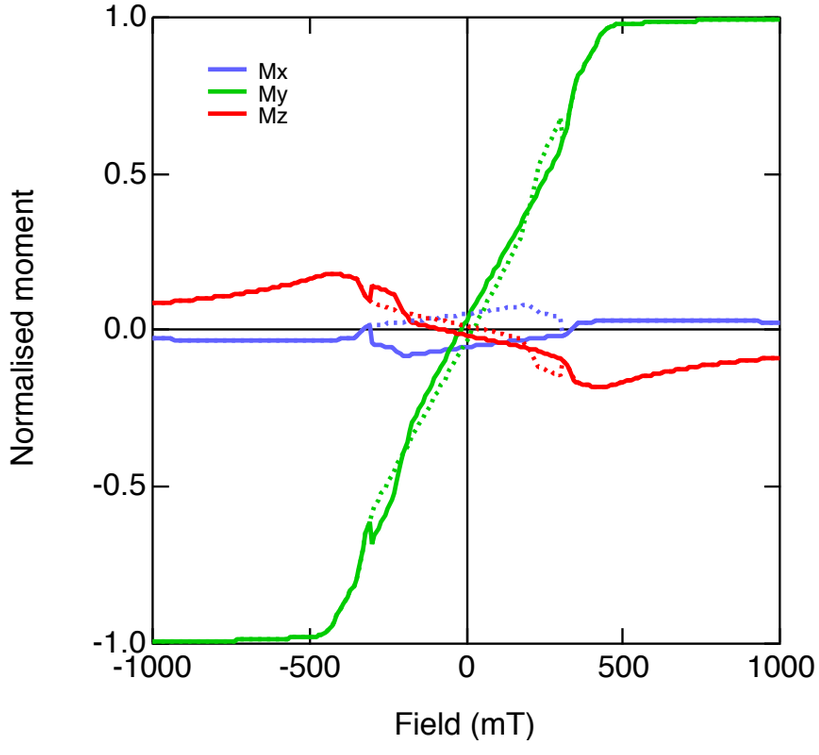

(c) Particle 48 // Z

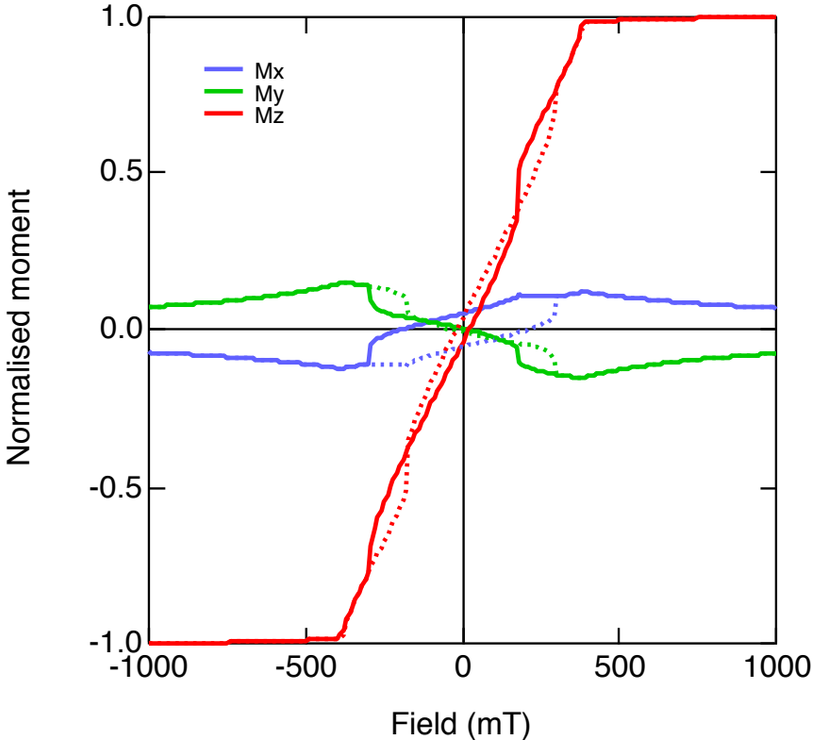

(d) Particle 233 // X

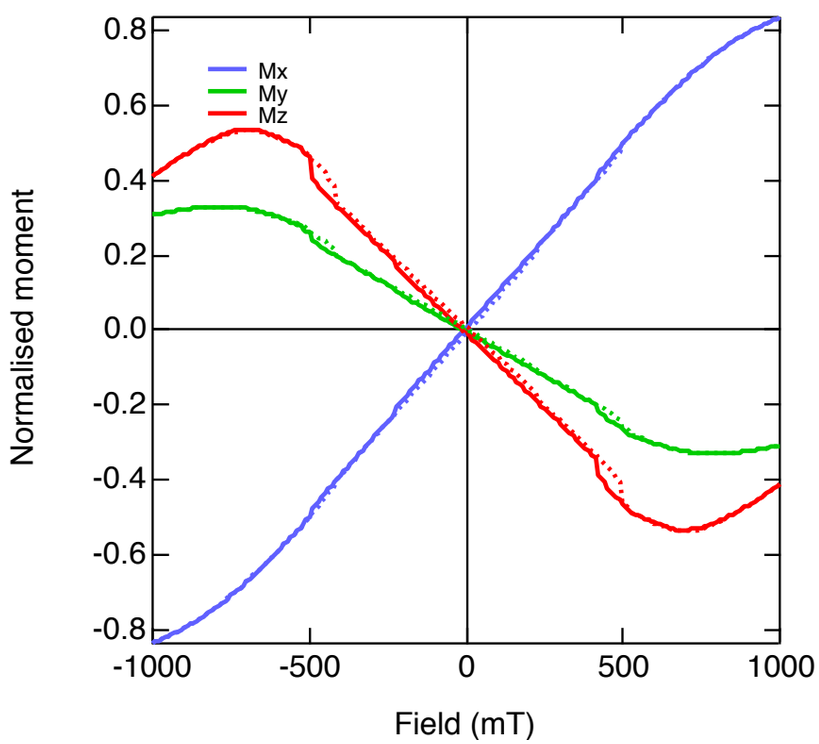

Figure 14